Search for a flux of cosmic-ray magnetic monopoles with an eight-channel superconducting detector

M. E. Huber,* B. Cabrera, M. A. Taber, and R. D. Gardner
Department of Physics, Stanford University, Stanford, California 94305
(Received 29 May 1990)

A superconducting detector for cosmic-ray magnetic monopoles originally designed with a cross section of 1.5 m^2 (averaged over 4π solid angle) for double-coincident events was active from 5 May 1987 to 5 August 1988. The detector consists of eight independent inductive gradiometers located on the surface of an octagonal prism. The conductor is niobium-titanium foil and the current sensors are rf SQUID's. The signal-to-noise ratio for a single Dirac charge is greater than 50 in a 0.05-Hz bandwidth, and low-noise data was obtained over 547 days of continuous cryogenic operation. Of this time, we obtained $\sim 50\%$ live time. Open circuits in portions of two gradiometers and occasional coupling of disturbances in adjacent gradiometers reduce the active sensing area to 1.1 m^2. A closed-cycle helium liquefier eliminates helium transfers and increases the stability of the data. Anticoincidence instrumentation includes strain gauges, a flux-gate magnetometer, an ultrasonic motion detector, and a wideband rms rf voltmeter. The exposure to date represents a limit on the flux of cosmic-ray magnetic monopoles of 7.2×10^{-13} $cm^{-2}s^{-1}sr^{-1}$ at a 90% confidence level, eliminating most of the phase space for monopole plasma oscillation theories.

I. INTRODUCTION

Grand unification theories [1] predict that magnetic monopoles exist with the Dirac magnetic charge $g_D = hc/4\pi e$ and a mass greater than 10^{16} GeV/c^2. The large mass precludes creating monopoles in accelerators, and even cosmic-ray monopoles are expected to be nonrelativistic. Under these conditions, superconducting detectors would provide the most convincing identification of a monopole in cosmic rays, since the response is independent of a particle's speed, mass, electric charge, and magnetic dipole moment [2].

A particle with magnetic charge g_D passing through a superconducting ring changes the flux in the ring by hc/e (the amount emanating from the monopole), which is twice the flux quantum of superconductivity, $\Phi_0 = hc/2e$. After the monopole has left the region of the ring, the flux change must be sustained by a persistent current in the ring. This current may be detected by an appropriate sensor, usually a SQUID (superconducting quantum interference device).

A candidate monopole event was observed [2] on 14 February 1982 in a single-inductor detector with a direct-coupling sensing area [3] of 10.1 cm^2 (all areas reported are the average over 4π solid angle). Since then, many superconducting detectors with coincident sensing areas on the order of 0.05–0.10 m^2 have been operated for periods as long as 3 years without observing any convincing candidate events [4–7]. A few groups have built larger detectors [8,9].

We have constructed an eight-channel detector with a sensing area of 1.1 m^2 for double-coincident events and a single-to-noise ratio of greater than 50 for a single Dirac charge [10]. The inductive element for each channel consists of two gradiometers wired in parallel. The detector was active over a period of 547 days, from 4 March 1987 through 1 September 1988, and we report on the design and operation in this paper. The first section describes the apparatus, including a general description of the geometry and details of the construction. The next two sections relate the operational details of the experiment, describing the support equipment, auxiliary instrumentation, and data-collection and analysis procedures. We end with a characterization of the detector response and the presentation of the data. The derivation of the induction matrix used to calculate the coupled response is included in the appendixes, along with the calculation of the gradiometer self- and mutual inductances.

II. APPARATUS

A. Design considerations

The rarity of monopoles presents three challenges in designing a detector. First, the monopole signature should be made highly unique so that the probability of a false positive signal is negligibly small. One approach, which we use, is to include multiple, independent inductors. Candidate events will consist of coincident signals from different inductors, with signal amplitudes consistent with that of a Dirac monopole. The number of coincident signals in a candidate event must also be consistent with the detector geometry. Our detector consists of eight inductors, each of which is connected to an independent SQUID.

Second, the detector area should be as large as is possible for a given cryogenic Dewar. A common geometry for detectors is therefore a convex volume with the inductive elements covering the surface. This geometry also aids in meeting the coincidence criterion above, since a monopole trajectory would intersect two and only two inductors. In our detector geometry, the detector induc-

tors are located on the surface of an octagonal prism with one inductor covering each face (Fig. 1).

Third, the detector should be as efficient as possible; that is, the ratio of true positive events to false negative events in the simulated detector response should be very large. However, there are practical limitations to detector efficiency. For example, the width of the inductor conductors is finite, and there are also small gaps between the conductors. Therefore, some monopole trajectories will intersect the conductors and produce fractional flux changes, and some will miss the inductors altogether. In addition, because the length of our system is much greater than its width, including detection loops on the ends for a marginal increase in detector area was not justified. This omission causes an additional loss in efficiency as some trajectories will penetrate one inductor and an uncovered end. In the end, we require all candidate events to be doubly coincident and consistent with a full Dirac charge.

Other design considerations include magnetic shielding requirements and the inductor configuration. A superconducting shield is required to attenuate external field variations, which can produce signals orders of magnitude larger than would a monopole. The magnetic shield in this experiment is a superconducting lead shell surrounding the detector (Fig. 1). The only openings in the shield are used for wires and pressure equalization, and each opening is shielded by an additional narrow lead tube in which external field variations decay exponentially. Any field existing at the time the shield becomes superconducting is trapped, but further changes in the external field do not couple to the interior field. The use of a gradiometer configuration also allows the sensing inductors to be located much closer to the magnetic shielding than would be possible with simple magnetometer inductors, thereby increasing the sensing area. The configuration is important because a monopole creates a flux vortex where it penetrates the shield, and the vortex fields in turn couple to the detector. The degree of coupling depends on the location of the trajectory, but on the average the net effect will be to reduce the size of the signal. Gradiometers are less sensitive than magnetometers to these fields, particularly if the cell size is no greater than the distance to the shield. The residual vortex coupling, however, still broadens the distribution of signal sizes slightly.

Somalwar *et al.* [11] noted that, for an inductor with a series inductance larger than the SQUID input inductance, the coupling to the SQUID is improved by subdividing the original inductor into smaller pieces, or units, and wiring these units to the SQUID in parallel. Parallel wiring of the units reduces the *fraction* of the current reaching the SQUID from a given unit since the current from one unit is split between the SQUID and all other units. However, the *total* current in a given unit is increased since its inductance is lower. There is a net gain, and the optimal signal is roughly proportional to $1/\sqrt{L}$ (where L is the self-inductance of the original inductor) rather than $1/L$, as it would be if the units were wired in series.

B. Detector dimensions and construction

The above considerations guided the detector design. The actual parameters were derived by maximizing the detector area subject to the constraints of maintaining a reasonable signal-to-noise ratio and restricting the spread in signal sizes resulting from vortex coupling. [12] The final inductor geometry is shown in Fig. 2 along with the inductor dimensions. As indicated, each inductor consists of two gradiometers, and the gradiometers are wired

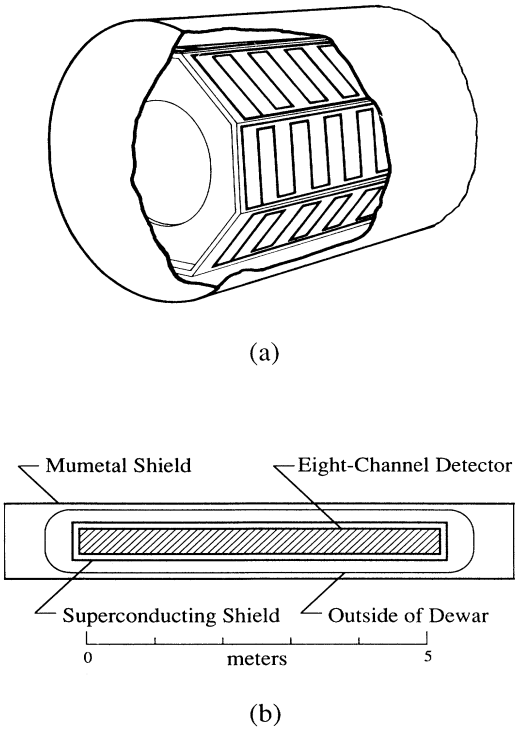

(a) (b)

FIG. 1. (a) Perspective view of inductors enclosed in the superconducting shield. (b) Schematic view of detector cross section, including Dewar and magnetic shielding.

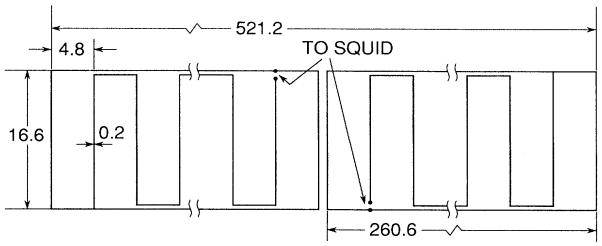

FIG. 2. Dimensions (in cm) and geometry of gradiometer detector inductors. The spacing of the central wire as it approaches the perimeter is 0.282 cm, center to center.

in parallel to the SQUID sensors. The gradiometers are composed of 27 balanced cells 9.65×16.6 cm large. Gradiometers on adjacent panels are offset by one-quarter of the cell length (2.41 cm) to reduce their mutual inductance. The inductance of the gradiometers is calculated in Appendix B and is 10.01 μH for the self-inductance of each gradiometer half and is 6.86 μH for the mutual inductance between gradiometer halves of opposite polarity. The characterization of the detector response is described later.

The physical apparatus consists of a fiberglass-epoxy (G-10) support structure, circuit boards, calibration coils, and magnetic shielding. The support structure contains six sections attached end to end. Each section has eight 1.3-cm-thick panels bolted to the edges of two 1.9-cm-thick octagonal bulkheads at each end. All screws and bolts used in the assembly are stainless steel to minimize magnetic contamination [13].

The detector circuit boards are 16.9 cm ×86.9 cm×0.16 cm G-10 sheets containing grooves 2.03 mm wide by 0.5 mm deep for the conductors. The conductors are Nb/Ti ribbon, 2.03 mm wide and 50 μm thick. The ribbon was obtained [14] in continuous lengths as long as 12 m, reducing the number of joints required. The tolerance on both grooves and ribbon was approximately 0.025 mm, and the ribbon width was slightly larger than the groove in order to form a slight cusp as it is pressed into the grooves. At corners, the foil was folded over itself at 45°, and at the joints, it was spot welded with multiple welds. Niobium blocks served as terminals to which the superconducting wires connected to the SQUID's were attached. A casting epoxy covered the ribbon to prevent motion, but the ribbon in the region near the welds and terminal blocks was not covered with epoxy. The twisted pair of superconducting wires leading to the SQUID's from each gradiometer is approximately 3 m long. The inductance of this length of wire is not negligible. Giffard, Webb, and Wheatley [15] have reported a self-inductance of 0.3 μH/m for a superconducting twisted pair, relatively independent of the wire diameter. Since we did not measure this inductance directly, the uncertainty in the twisted-pair inductance dominates the uncertainty in all other inductances in the detector. From calculations of the gradiometer inductances detailed in Appendix B, we estimate that the total load inductance seen by the SQUID for a complete panel is ~4 μH. This value is relatively well matched to the ~2-μH SQUID inductance.

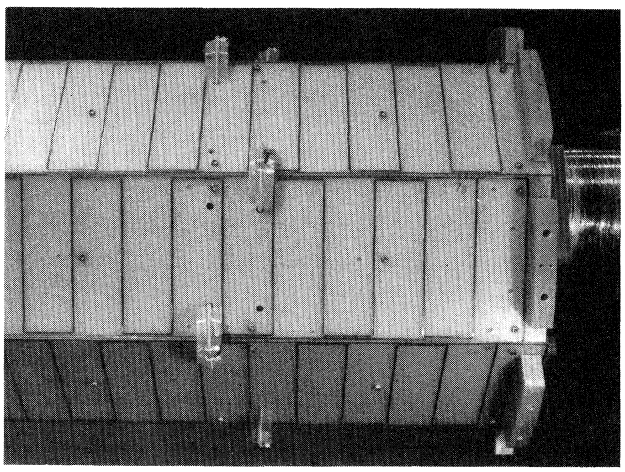

FIG. 3. Placement of calibration coils relative to the end of the detector.

With three circuit boards in each gradiometer, the foil must bridge the gaps between the boards. A strain relief loop at the gap accommodates the flexing in the support structure. A test verified that the G-10 contracts more than the foil, and so differential contraction should not further stress the foil. We discovered the need for these strain relief loops during the initial phases of the assembly. However, some circuit boards were already completed when the flexing was discovered, and strain reliefs were retrofitted only in those joints with significant gaps. We may have paid for this oversight, as a few of the conductors did break after cooldown.

C. Calibration coils

Toroidally wound coils allow application of known fluxes to the inductors for calibration (Fig. 3). The coils are No. 32 wire wound on a 20.3-cm length of No. 10-32 threaded nylon rod and joined into a toroid with an aluminum plug. The coils are located in the sixth and seventh half-cells from each end of the detector. All calibration coil leads entering the detector region are filtered through high-frequency electromagnetic-interference- (EMI-) suppression filters. The calibration coils share a common ground. Each calibration coil is individually accessed through a room-temperature switching network. This arrangement restricts the combinations in which the coils may be stimulated, but can be bypassed if necessary. Each calibration coil couples to two adjacent gradiometers simultaneously, and coils are at both ends of the detector. This arrangement produces four directly coupled signals per channel, one for each half of each gradiometer. A current of 0.19 μA through the coil (obtained by applying a voltage of 0.38 V across the coil and a series 2-MΩ resistor) produces a flux equivalent to that of a Dirac monopole (Fig. 4). Calibration results are used to determine the gradiometer inductances and, hence, the response function (Appendix A).

D. Shielding

The superconducting shield is supported by a thin (0.8-mm) G-10 sheet wrapped around G-10 forms with a 25-cm radius. The strength of the bent sheet is sufficient to support the weight of the shield, a 0.8-mm sheet of roofing lead which covers the entire detector. All joints are soldered to provide superconducting continuity. The electrical leads for the SQUID's and calibration coils exit at opposite ends and are routed through long, narrow lead tubing approximately 3.2 mm in diameter. The magnetic fields along such a tube are attenuated exponentially along the length, and all tubes are at least 10 times longer than their diameter. A 5.1-cm-diameter hole at each end

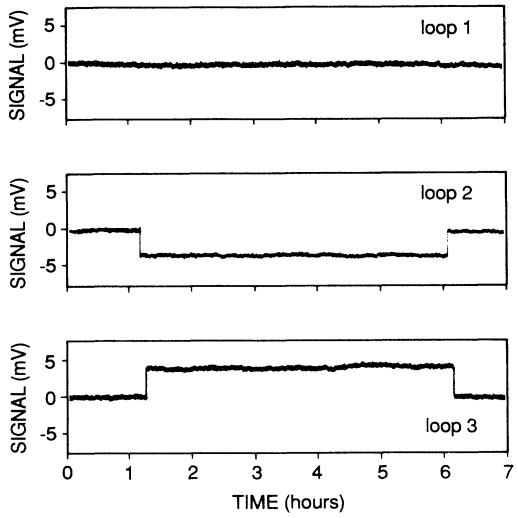

FIG. 4. Calibration signal equivalent to one Dirac charge in inductors No. 2 and No. 3.

(again with a long superconducting tube for attenuation of external fields) reduces the pumping time and pressure stress on the shield during evacuation. The holes do not degrade the shielding.

The shield was also inspected prior to insertion into the Dewar for pinholes, and those which were found were then filled with solder. To protect the shield from tears during insertion into the Dewar, Teflon skids were attached with external straps to the outside of the detector at each bulkhead.

Sheets of a high-permeability shielding material (mumetal) surround the detector. The mumetal shield is not a continuous sheet, but consists of 253 cm$\times$72 cm$\times$0.89 mm sheets bent into a rosette with an average radius slightly greater than 56 cm. Additional strips in direct contact with the large sheets cover all gaps with a 5-cm overlap. Four holes approximately 6 cm in diameter are at the bottom for the Dewar stands, and one hole approximately 40 cm in diameter is at the top for the gas handling fittings. Ten degaussing strips run the length of the Dewar and are spaced equally around the circumference. The main shielding extends only to the end of the open Dewar, but additional open-ended caps extend the shielding by 126 cm, so that the ends of the detector are recessed by at least 1.2 m from the ends of the external shielding. The field was measured during assembly (before the detector or end caps were installed) both before and after degaussing at various positions in the Dewar. The field in the region of the detector was measured at less than 20 mG. Figure 1(b) shows the position of the shield relative to the Dewar.

E. SQUID sensors

The current sensors are rf-biased SQUID's [16] operating at 190 MHz [17]. Each SQUID is mounted in a G-10 tube on a brass base (Fig. 5). The rf matching network is located in this piece, and there is a 3-Ω rf shunt across the input terminals. The SQUID's are twice shielded, with a niobium cylinder and lead-plated brass outer shell. The complete assembly is mounted to the copper reservoir of a standpipe on the helium system for efficient heat sinking (Fig. 6). Epoxied into copper housings, 100-Ω metal-film resistors are attached to each SQUID to locally warm and cool each SQUID through its transition temperature. This procedure sometimes reduces the noise level, but is not used often.

Flexible coax connects the SQUID's to the vacuum feedthrough plate at 4 K, and stainless-steel semirigid coax is used between the 4 K surfaces and room temperature to minimize the heat leak. The semirigid coax is heat sunk to the radiation shields with loops to increase the thermal length. The extra length could be added since the tuning characteristics of the SQUID's are nominally independent of the rf line length. The units containing the rf and feedback electronics are connected to

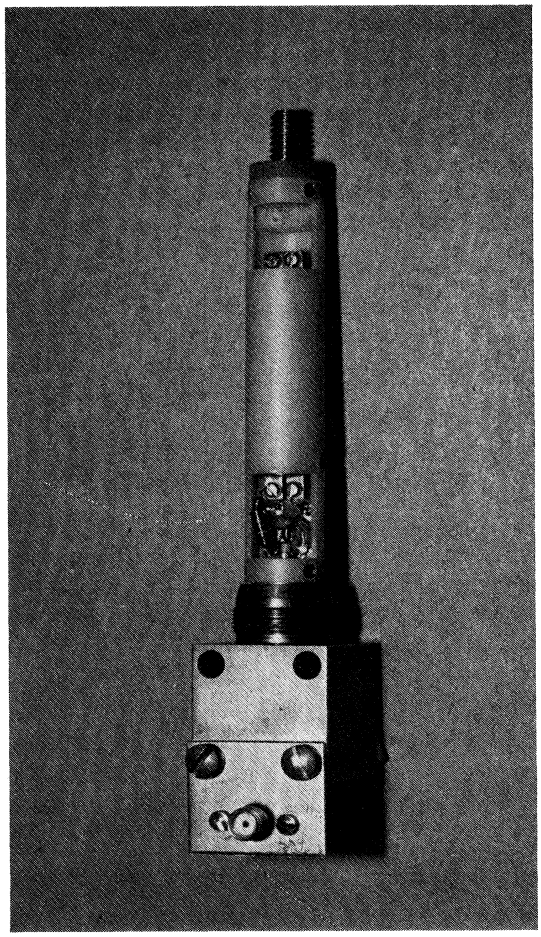

FIG. 5. SQUID housing and mounting assembly. Only the bias and input terminals of the SQUID are visible; the rest of the SQUID is hidden by the G-10 housing. The rf matching network is at the center of the photograph, and the brass cube at the bottom is used for mounting and heat sinking. The input leads enter the assembly through the hollow niobium screw at the top.

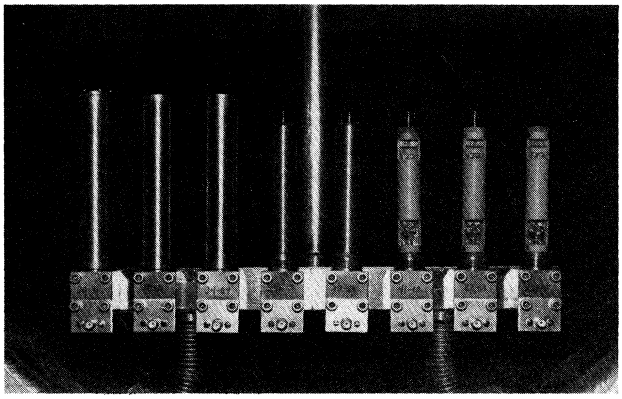

FIG. 6. SQUID's in various stages of assembly in position on the Dewar standpipe (used for cooling). SQUID's at right are in the same stage of assembly as shown in Fig. 5. At center, the niobium shield has been installed, and at left, the assembly is completed with a lead-plated brass cylinder.

the Dewar, with the control units located in a nearby instrument rack. The feedback electronics were modified by decreasing the slew rate in order to reduce the frequency of jumps between flux states in the SQUID caused by impulsive noise.

The calibration parameters for the SQUID's are listed in Table I. The current and voltage sensitivities are reported on the manufacturer's calibration sheets. For all but two of the SQUID's, the input inductance is inferred from noise parameters on these sheets. For the remaining two, which were used in a previous experiment, the input inductances were measured directly during that experiment.

III. SUPPORT EQUIPMENT AND AUXILIARY INSTRUMENTATION

A. Cryogenic Dewar

The Dewar is a horizontal cylinder containing three separate regions: experimental, helium, and thermal. The experimental compartment is at the center and surrounded by an annular region containing liquid helium. The boil-off gas cools two nested radiation shields in the thermal vacuum before venting. The shields are separated by plastic spacers. The experimental region, which weighs ~680 kg when loaded with the detector and liquid helium, hangs from two uniaxial fiberglass/polyester rods 15.2 cm long and 0.5 cm in diameter. The estimated heat leak is 22 mW per rod.

A standpipe between the top and bottom of the annular helium chamber provides support and cooling for the SQUID's and contains the helium level sensor, a 30-cm continuous-level probe. Two carbon resistors at the top and bottom of chamber serve as limit indicators. The 30-cm probe is able to monitor the helium level from ~25% to ~75% of the ~200 liter capacity.

Sixteen carbon resistors monitor the temperature at various points in the Dewar during cooling and warming. Ten are mounted on the experimental region and radiation shields: three at the top, three at each end, and one on the support point. There are two on the rf feedthrough heat sinks, one on a SQUID base, and three on the lead shield of the detector array.

Thermocouple pressure gauges monitor the experimental region and thermal vacuum, and an ion gauge also monitors the thermal vacuum. A pressure transducer monitors the helium pressure for regulation. Between 1 and 2 torr of helium (at room temperature) is in the experimental compartment as exchange gas during cooling. A leak which opened during the cooling has drawn off this gas and the detector now operates in a vacuum. The detector cools to nitrogen temperatures in less than 3 days with 700–800 l of liquid nitrogen and reaches helium temperatures in less than 1 day with 500 liters of liquid helium. The rate of helium evaporation is between 0.5 and 0.8 liquid liters per hour.

B. Helium liquefier

The Dewar is connected to a closed-cycle helium liquefier. The liquefier eliminates the need for helium transfers, reducing helium costs and improving the stability and quality of the data. The liquefier compressor is located in an adjacent room to minimize noise and mechanical disturbances.

TABLE I. Calibration parameters of SQUID's by panel number. All self-inductances except the first and last entries are inferred from data on the calibration sheets supplied by the manufacturer; the remaining two were measured prior to use in the three-axis experiment.

Panel No.	SQUID serial No.	L_s (μH)	I_s/Φ_0 (nA)	V/Φ_0 (V)	I_s/V_0 (nA/V)
1	271879-03	2.31	92.9	2.15	43.2
2	271931-08	1.50	115.	2.20	52.3
3	271934-04	1.97	101.	2.21	45.7
4	271941-10	2.00	100.	2.05	48.8
5	271950-07	1.69	109.	2.04	53.4
6	271930-12	2.05	99.	2.05	48.3
7	271930-11	2.17	96.	2.07	46.4
8	271879-06	2.48	89.6	2.01	44.6

The liquefier capacity is about 5 liquid liters per hour, more than sufficient for the load from the Dewar. The liquefier regulates the liquefaction rate by heating the Joule-Thompson valve when the Dewar pressure falls from over-liquefaction. A pressure transducer senses the Dewar pressure and a feedback circuit controls a programmable power supply connected to the heater. The Dewar pressure and temperature is constant for extended periods, limited only to small daily drifts, believed to result from atmospheric pressure variations and other refrigerator instabilities.

C. Anticoincidence instrumentation

Three ceramic strain gauges monitor detector motion, which can cause spurious offsets. One is located at the top of the experimental region on the gas-handling flange and the others are located at each end of the detector, mounted on the lead shield. A thin Mylar sheet isolates them from the metallic surfaces, and varnish is used as an adhesive. The leads are filtered by high-frequency EMI-suppression filters both at room temperature and 4 K. Only one strain gauge is monitored at a time, usually the strain gauge at the SQUID end of the detector. A charge amplifier is used as a preamplifier.

Two factors contribute to making discrimination of mechanical disturbances difficult. First, the Dewar rests directly on the concrete floor, which is not isolated from the rest of the laboratory, and there are many background disturbances. Second, the detector has many vibrational modes, and the frequency spectrum of external hammer taps to the Dewar has a complicated structure. We have found that a six-pole bandpass filter with corners at 90 and 120 Hz appears to maximize the response to external taps. The root-mean-square value (with a 0.016-sec time constant) of this output is filtered at 10 Hz with a two-pole filter.

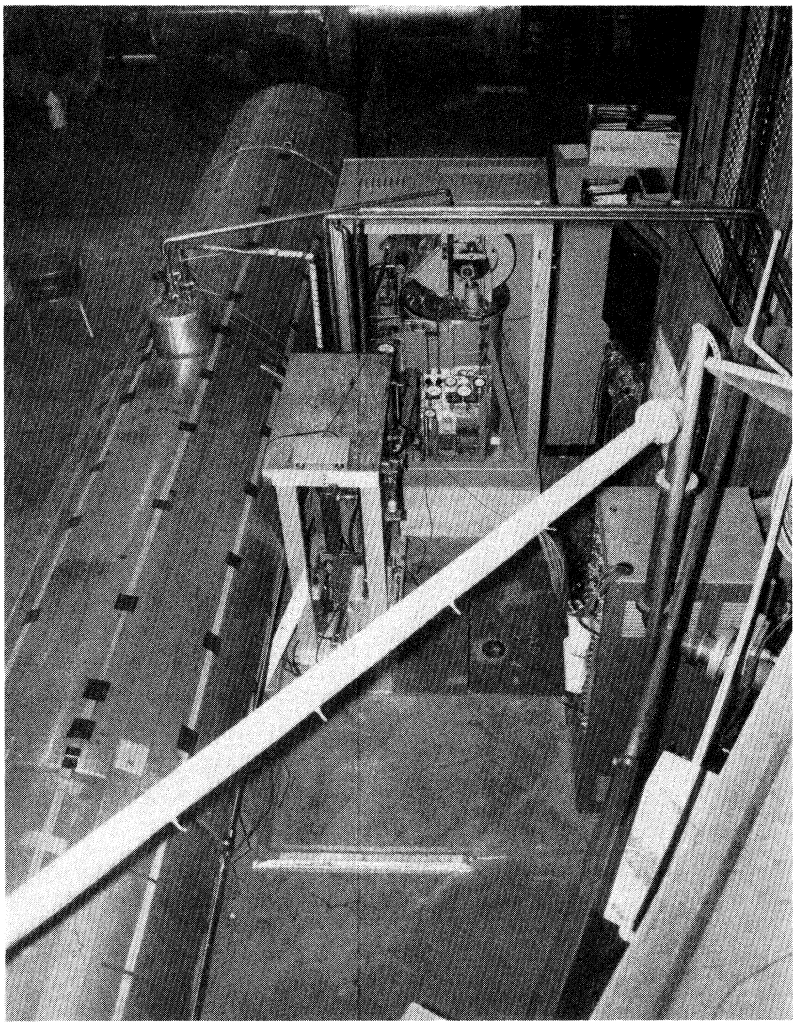

FIG. 7. Overview of detector laboratory. The helium liquefier is the large box at the center, and the shielded Dewar runs top to bottom along the left side of the picture. The ultrasonic motion detector is at the top of the wooden assembly in front of the liquefier and detects motion over an area from the front end of the Dewar to the electronics rack. The compressor for the liquefier is located behind the wall in the lower right corner.

A flux-gate magnetometer monitors the external fields in the 1–10-mG range. There are no significant correlations between external disturbances and SQUID offsets, even when the "disturbance" is a 4-ton forklift operating less than 2 m from the detector. As a result, the magnetometer was replaced with a wide-bandwidth rf voltmeter, which another group [18] has reported as being more sensitive to those disturbances which actually affect the SQUID output. There have been too few SQUID offsets since the rf voltmeter was installed to determine any correlation to the rf level.

The data-acquisition system monitors three digital data lines. A veto switch inhibits the storage of high-speed data (discussed in the next section) on those occasions when we perform maintenance work known to cause SQUID offsets. The other anticoincidence instrumentation is used in subsequent analysis, so it will not prevent triggering of the high-bandwidth data. An ultrasonic motion detector monitors laboratory activity along the path leading to the SQUID electronics (Fig. 7). A power line monitor records any disturbances in the 110-V power for the experiment. The monitor is most useful for voltage spikes or brownout conditions, since these variations are small and might otherwise go unnoticed.

IV. DATA COLLECTION AND SEARCH PROGRAM

A. Data collection

Two strip-chart recorders and a computer store data in both analog and digital formats, respectively (Fig. 8).

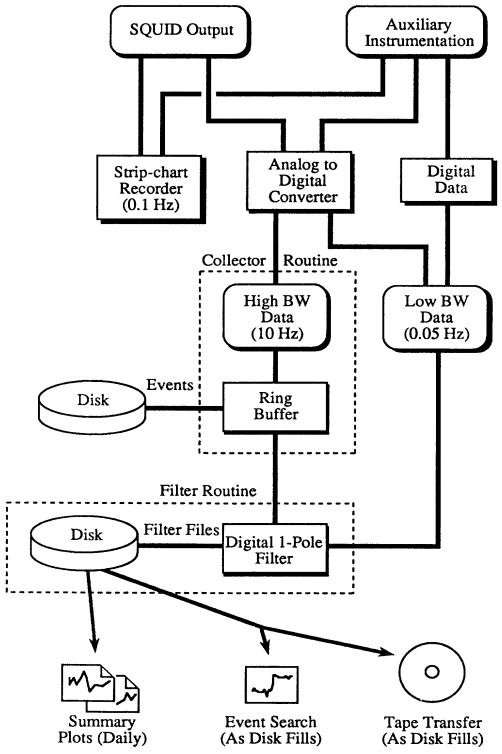

FIG. 8. Flow chart of data-acquisition system, which contains both analog and digital recorders.

The strip-chart records contain data from the eight SQUID's and three auxiliary channels, all of which are filtered through a single pole low-pass filter with the pole at 0.1 Hz.

The computer is a Digital Equipment Corporation PDP-11/23 running the RSX v4.1 operating system. A twelve-bit analog-to-digital converter samples twelve analog signals (eight SQUID's and four auxiliary instruments) at two rates. The first is 20 samples per second for the SQUID's and two anticoincidence sensors (magnetometer/rf voltmeter and strain gauge) and the second is one sample per 10 sec for two status sensors (helium level and pressure). The high-speed data are stored in a ring buffer and digitally filtered by a single-pole algorithm with a 0.05-Hz corner frequency [19]. The filtered data and low-speed data are stored on a disk, and each file contains 8 h of real-time data. The high-

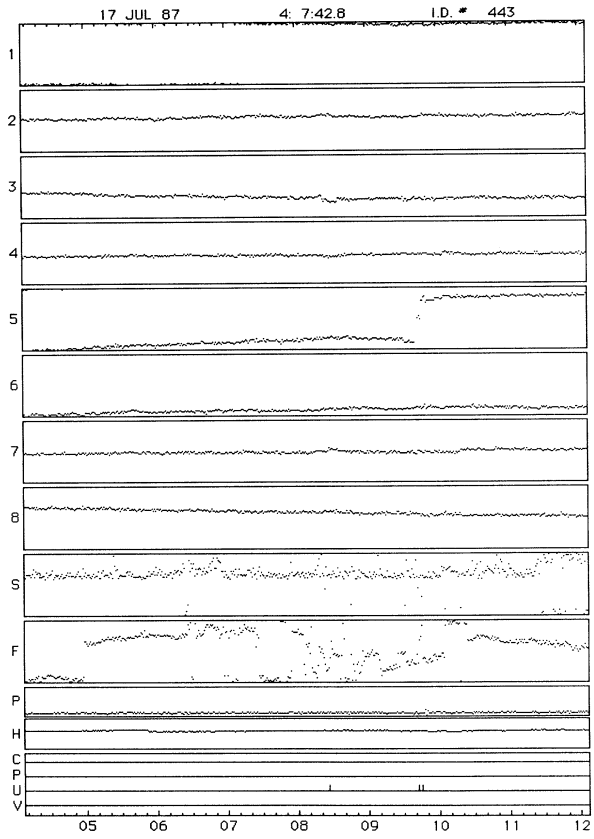

FIG. 9. Summary of 8-h data file. The top eight rows contain filtered data from the SQUID's ($2.5g_D$ change full scale). Rows *S* and *F* contain filtered data from the strain gauge (arbitrary units) and flux-gate magnetometer (0.2-mG change full scale), respectively. Rows *P* and *H* contain unfiltered low-frequency data from the pressure monitor (2 cm of H_2O change full scale) and helium level sensor (16 cm change full scale), respectively. The last row contains digital data from a cosmic-ray channel (unused), power line monitor, ultrasonic motion detector, and event veto. Only one in every sixth point is plotted on each trace.

speed data are saved on a disk only when an offset occurs in the filtered data. Data from three digital channels are sampled at the lower rate and contain information concerning veto status, power line disturbances, and motion in the laboratory. A system log file records system and collector status events such as missed interrupts, changes in the veto state, and occurrence of the offset events, along with the time of each.

Data summaries are plotted daily for each 8-h file (Fig. 9). Most spurious events can be identified from these records or a combination of these records and the chart recorder output. Other programs are available to analyze the data in more detail if necessary. When offset events occur, summaries of those data files are plotted as well (Fig. 10). Simultaneous offsets in a SQUID and either auxiliary channel are easily identified in these records.

Over a period of time, the data fills the disk and are transferred to magnetic tape for long-term storage. This process is repeated every 2–3 weeks depending on the number of high-density data records.

B. Search program

A digital search for monopole-like events (step offsets) in the stored data is used to quantify the live time and offset sizes. Enough points are stored in an array to include approximately twice the time window required in the test for a clean offset. This array contains four main segments, two regions together called the "active buffer" on either side of a test point, used to determine the data quality, and an additional region on both sides of the active buffer, used to ensure that no more than one event occurs in a given interval (Fig. 11).

Two criteria must be met to include data in the live time and one additional criterion must be met to identify a valid event. First, the data must have a low-noise level. The noise level is defined (for this purpose) as the maximum difference between any point in the buffer and the average value of the buffer as a whole, and the noise level for live data may not exceed the *noise threshold.* This criterion also prevents offsets superimposed on a ramp from

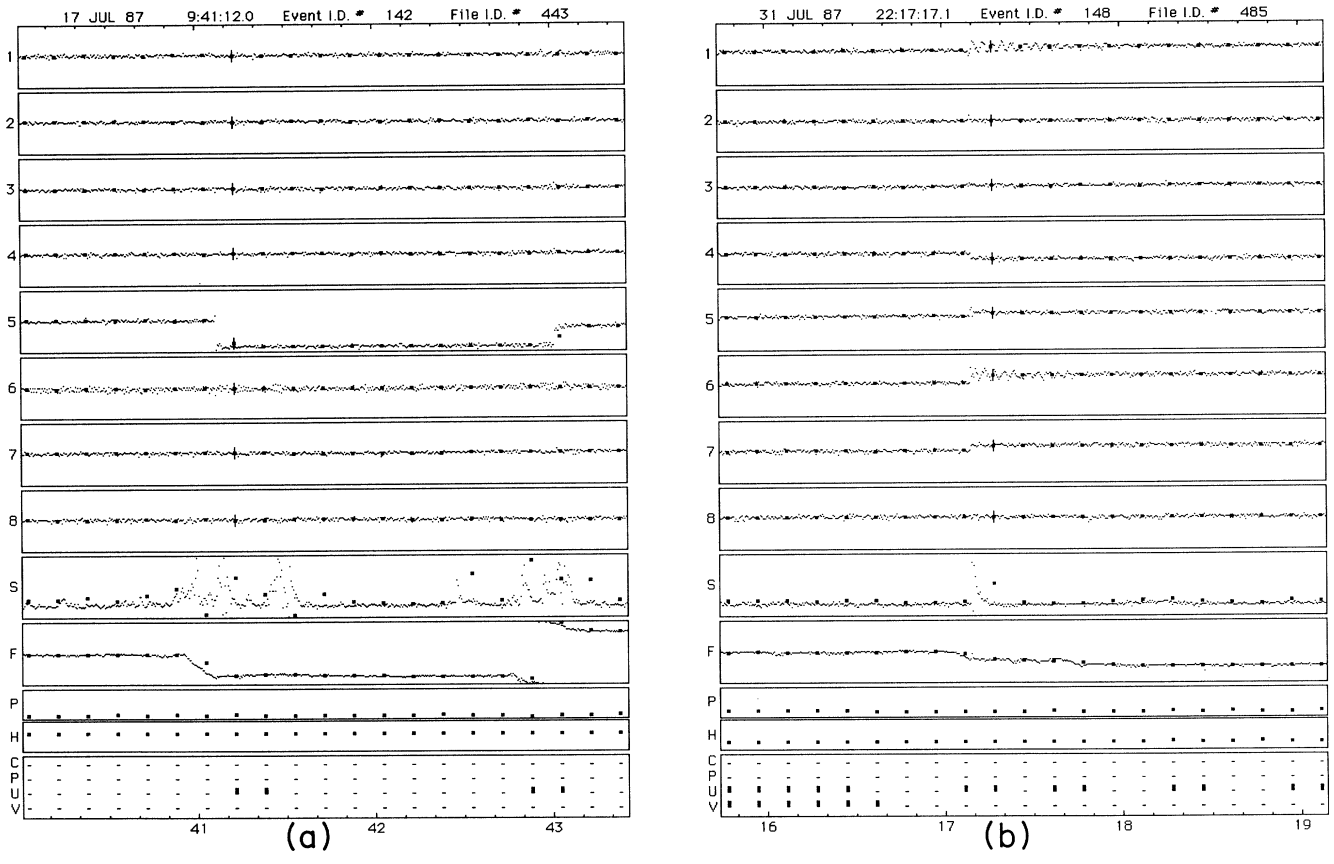

FIG. 10. (a) Summary of event data file. The row identification is as in Fig. 9 except that the full scales now correspond to $12.5g_D$ for the SQUID's, 0.8 times as sensitive for the strain gauge and 0.5-mG change full scale for the flux gate. Unfiltered data is shown as small data points; filtered data is superimposed as large data squares, and the event trigger point is marked with a vertical bar. The event shown occurred at approximately 9:41 in the file shown in Fig. 9. Note the coincidence between signals in the SQUID with signals in the strain gauge, magnetometer, and motion detector. Only one in every eighth point is plotted on each trace. (b) Event data file demonstrating resolution of SQUID sensors. Note the oscillations in the SQUID output resulting from the sharp disturbance recorded on the strain gauge.

being identified as events. Second, the difference between consecutive points in a buffer must not exceed an *offset threshold* unless the offset also qualifies as an event. This requirement prevents identification of slow rises in the data as events and prevents frequent offsets from being included in the live time. The last criterion is that, if the data are quiet and there is only one offset in the buffer, the difference between the averages of the buffers on either side of the offset must be greater than the *event threshold* for final identification as an event. This test excludes data which consist of a rapid rise and fall in signal size (spike). The algorithm incorporating these criteria is represented in Fig. 12. For various reasons, the tests are not performed in the exact order described above.

There is a slight complication in that the offsets are digitally filtered and not exact step functions. In large events, there could in fact be two or three consecutive points with large offsets, owing to the exponential rise time in the filter response. Therefore, a few points after the first offset are ignored before beginning the second buffer. These points are shown in Fig. 11.

All SQUID channels must be live simultaneously to include the data in the operational time. If a single channel is noisy, the other channels could still be active, but the detector area is different for each situation since the noisy channel cannot contribute to the sensing area. Hence the data from all channels is discarded if the data from any one channel are unacceptable.

The search algorithm spans contiguous 8-h data files. However, a few points at the ends of continuous data-collection periods (when the collector is first started or stopped) do not contribute to the live time since the test buffers cannot be filled. This lost data are a small fraction of the total.

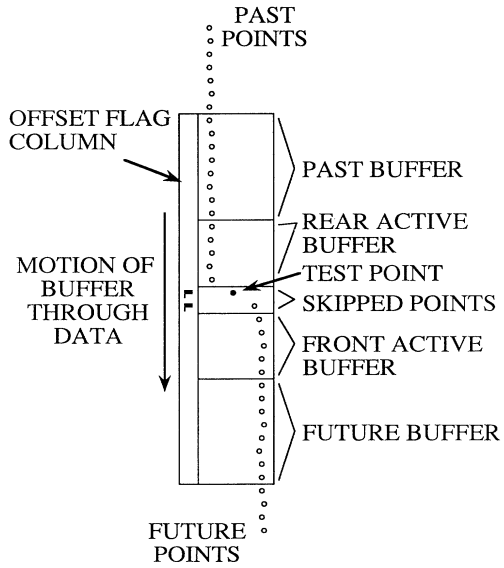

FIG. 11. Schematic representation of buffers in the event search algorithm (data is simulated).

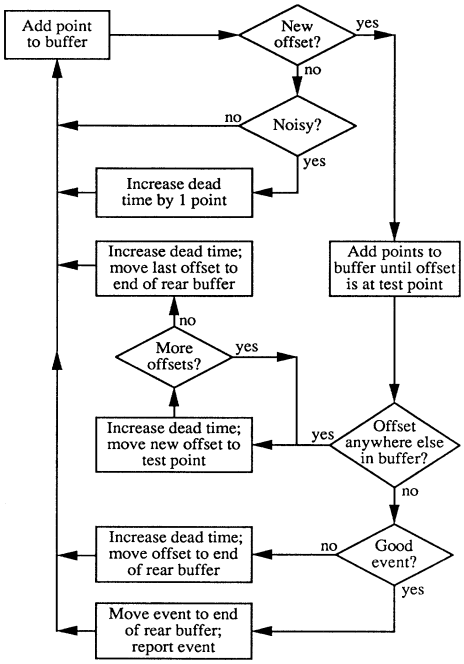

FIG. 12. Flow chart of algorithm to search for events in the filtered data. Execution begins in the box at top left and proceeds through the loop until the end of the file is reached. Special routines test the beginning and end of a file. See text for the definitions of offsets, noise, and events. The criteria for an event include low noise and a minimum difference between buffer averages.

The search algorithm was tested on obviously pathological files to verify its accuracy and on normal files to set the three independent thresholds, for noise, offsets, and events. The current buffer size is 123 points (1230 sec) with three points skipped for filtering effects. The noise threshold is 0.54 mV, the offset threshold is 0.77 mV, and the event threshold is 0.31 mV. For reference, the nominal signal for a Dirac monopole is about 3 mV. The algorithm produces total and live hours for each channel, the minimum live time for all channels, and events with the time and magnitude of their occurrence.

V. CHARACTERIZATION

A. SQUID noise

The noise levels are very uniform between SQUID's, and the spectra are flat above 0.1 Hz as determined by a spectrum analyzer. The measurements of the white-noise level at 1.0 Hz with the detector inductors connected are plotted in Fig. 13. This noise is within the BTi specifications for shorted SQUID performance. The calibration coils provide an independent measure of the noise levels, through measurement of the fluctuations observed in offset magnitudes during calibration tests. Using a stable function generator with a long-period square wave, a $10g_D$ calibration signal was applied to channels 1 and 8 repeatedly, over several hours, producing 25 offsets in

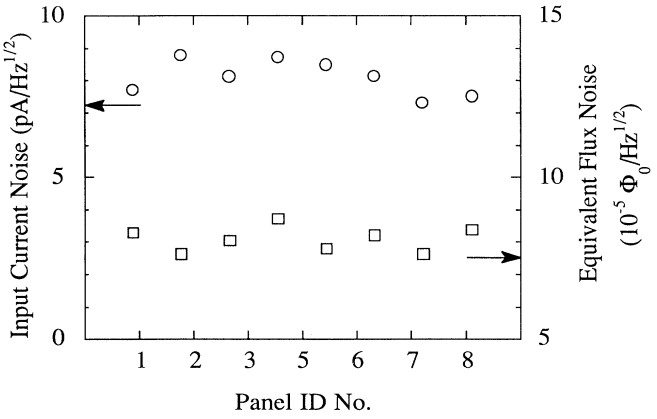

FIG. 13. Equivalent input noise at the SQUID at 1 Hz with the inductors connected. The flux noise amplitude is referred to the flux quantum in the SQUID.

each channel. The search program determined the offset amplitudes, and the fluctuation in these amplitudes is a measure of the noise in the bandwidth of the digital data. This value is important since the noise levels begin to rise just below the lowest frequency measurable with the spectrum analyzer.

The signal sizes in each channel were slightly different (owing to coupling effects to be discussed later), but the standard deviations were quite close. The standard deviation for channel No. 1 was 2.96 pA and for channel No. 8 was 3.26 pA. By subtracting the average signal for the appropriate channel from the individual signals, deviations from the mean for both channels can be plotted on the same graph (Fig. 14). The standard deviation of this distribution is 3.1 pA. For signals between 160 and 180 pA ($\sim 1 g_D$), the average signal-to-noise ratio is greater than 50. The ratio might be slightly less for some signals since the signal size varies from channel to channel owing to inductance and SQUID-gain variations. The standard deviation calculated from the white-noise values measured by the spectrum analyzer is 2.4 pA and is superimposed on the data in Fig. 14 [20]. The standard deviation for the calibration data is larger since the noise is greater than the white noise at frequencies below 0.1 Hz.

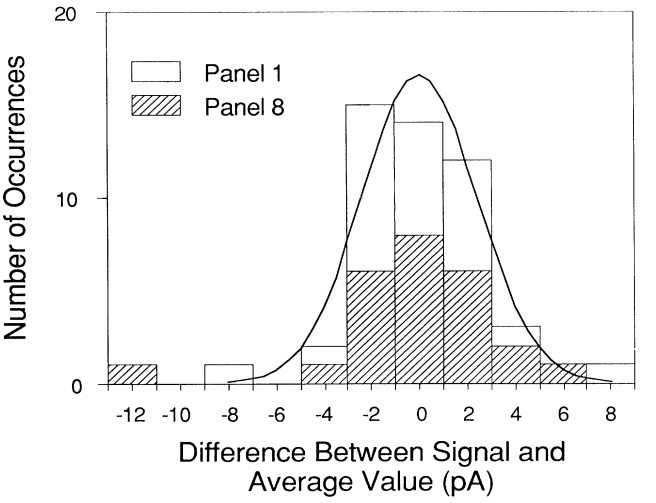

FIG. 14. Histogram of results from multiple calibration measurements. Results from two panels are shown. Because the signal sizes are not equivalent, the average for each panel has been subtracted from the values before plotting. Superimposed on the data is the distribution inferred from direct measurements of the high-frequency SQUID noise.

B. Detector response

We developed two models to describe the interaction between the detector and a magnetic charge, with each model emphasizing different aspects of the interaction. With the first model, we describe the interaction of the flux vortices trapped in the shield with a detector consisting of identical, uncoupled gradiometers. With the second, we calculate the signals produced by magnetic charges in a detector with coupling between adjacent gradiometers (adjacent-panel coupling) and selected inactive gradiometers, but in the absence of shielding.

The first model of the detector consists of identical, ideal gradiometers in which the wire width is finite and there is no gap between the center and edge wires; a superconducting shield also surrounds the detector. With this model, we calculate the effect of the shield and wire width on the distribution of signal sizes. In a numerical simulation, a random number generator produces an isotropic three-dimensional distribution of over 80 000 monopole trajectories. For those trajectories which intersect the shield, the points of intersection with the shield and (if appropriate) the detector are calculated for entry and exit. The algorithm then determines which section of which gradiometer was penetrated, whether or not the monopole hit a wire (and, if it did, where on the wire it hit), and the magnitude of the coupling from the vortex fields. To decrease computation time, the flux coupling was calculated first for various vortex positions relative to the grid and then stored in a table for later reference. A contour plot of this coupling is shown in Fig. 15. An earlier version of this procedure was used to characterize the response of the three-loop detector [3].

The calculations excluded certain edge effects, such as vortices in the shield end plates and the excess vortex coupling at the ends of the gradiometers. The first is safely ignored since the gradiometer is further from the shield end plates than it is from the rest of the shield, and the second since those trajectories represent less than 2% of the sensing area.

From these calculations, we obtain the distribution of signal sizes for an isotropic monopole flux (Fig. 16). The width of the distribution is a measure of the discrimination against non-Dirac signals. The enlarged region shown in Fig. 16(b) contains trajectories which penetrate two inductors cleanly. The rectangular regions of lower density contain trajectories which penetrate one inductor cleanly, but intersect the wire of the second inductor.

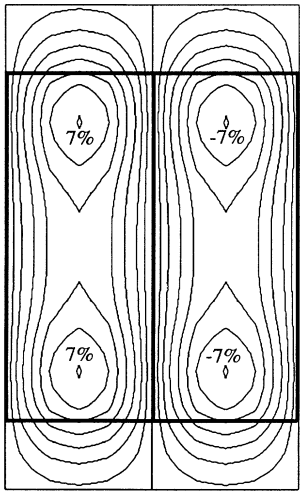

FIG. 15. Contour plot of flux coupling to detector from vortices in the shield. A single gradiometer cell is shown. The contour lines (every 1%) represent percentages of g_D. The plot extends past the edge of the gradiometer cell since the shield flux from a monopole penetrating an adjacent panel can still couple to the cell shown.

The linear regions near zero signal in one or two inductors contain trajectories which penetrate one inductor and the uncovered detector ends. Only trajectories in the enlarged region would be considered as candidate events. We do not include signals from the vortices alone in the sensing area.

We also verify the detector area for double-coincident events with this simulation. The sensing area is the ratio of the number of trajectories which penetrate two inductors to the total number of trajectories multiplied by the area of the region from which the random points were selected. The area determined by this means agreed with the analytic calculation, 1.5 m^2. The actual sensing area is smaller, however, since (as we discovered from the calibration data) some gradiometers or gradiometer sections are inactive. An open circuit in one gradiometer for channel No. 4 renders that segment inactive, although the other gradiometer continues to operate. The data indicate that the break is in the central conductor rather than in both edge conductors. Only one-half of one gradiometer for channel No. 6 is inactive, indicating a break in the edge conductor. The other half of the gradiometer is responsive, but now operates as a magnetometer rather than a gradiometer. We observe no resulting increase in the noise, and simple calculations indicate that the vortex coupling will be on the order of $-0.4g_D$. The complete signal from a monopole penetrating the active half would thus be approximately $0.6g_D$, large enough to include the area from this half of the gradiometer in our area calculations. Modifying the model to include the inactive circuits reduces the total sensing area for double-coincident events to 1.31 m^2.

The second model of the detector includes adjacent-panel inductive coupling between gradiometers, but does not include shielding effects. The actual geometry of the gradiometers is accurately represented in the inductance calculations (detailed in Appendix B), and the calculations of the detector response include the effect of inactive segments (Appendix A). With this model, we calculate the signal sizes in the absence of shielding for comparison with the calibration data. The calibration results do not agree exactly with the calculations (Fig. 17), but there is a strong correlation between the signal sizes and the coupling symmetry of the segment which was excited (see Fig. 22; a detailed description of the coupling symmetries listed in the figure is also given in Appendix A). Also, signals in panels with broken conductors (4 and 6) are in good agreement with the model. The agreement in panels 4 and 6 confirms that the four couplings selected for the later variational calculations accurately describe the basic detector interactions. We have excluded most possible explanations of the discrepancies (including vari-

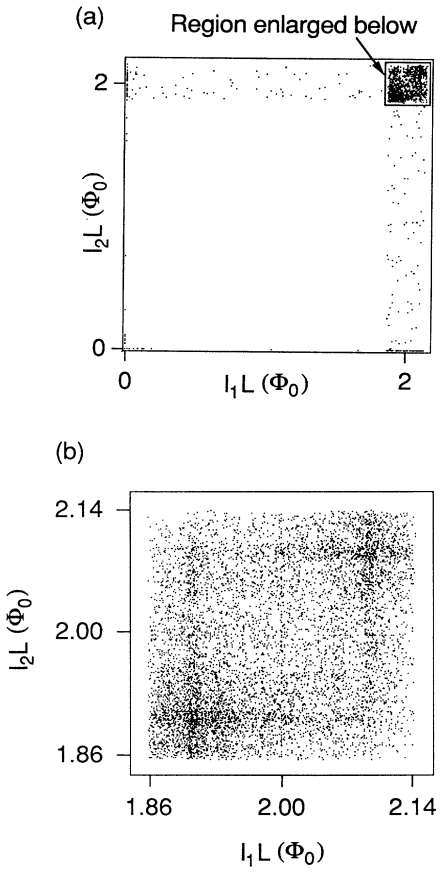

FIG. 16. Detector response function for a uniform distribution of monopole trajectories. (a) Each dot represents one trajectory and the signals it causes in the two closest inductors. Signals with a near-integer value in one inductor and a smaller value in the second result from trajectories passing through a wire in the second inductor. The spread around $2\phi_0$ is due to the flux vortices coupling to the shield. (b) High-resolution plot of region representing trajectories penetrating two inductors.

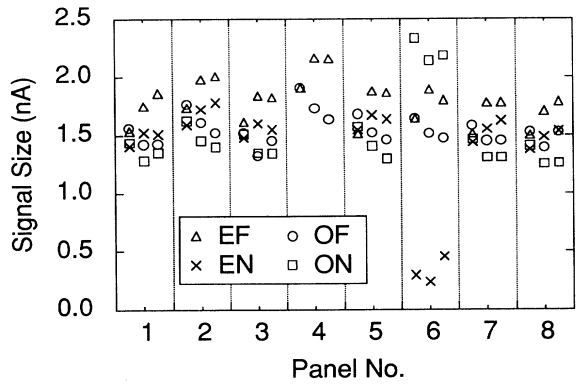

FIG. 17. Summary of calibration results. Each symbol represents one of the four calibration symmetries described in the text. The first column for each panel contains values calculated with no adjacent panel coupling and no inductance variations. The second column contains values calculated with adjacent panel coupling and inductances resulting from a six-parameter error minimization. The third column contains the observed values.

ations in the calibration coils or gradiometer parameters and various shielding effects) and believe the most likely cause is changes in the inductances caused by the slight magnetization of stainless-steel assembly screws [13], which are located in a regular pattern. To obtain the best estimate of the detector response, we perform a variational calculation in which the inductances vary according to the observed coupling symmetry, minimizing the least-squares difference between the calculated and observed calibration signals. A variation of only 7–13 % in the inductances, in a six-parameter fit, substantially improves the agreement (Fig. 17). The final result is a table of expected signal sizes as a function of which gradiometer half, or section, the monopole penetrates (Table II). The spread in signal size induced by vortex coupling from the shield is not included in this model, and the actual signals may therefore vary from those in the response table by up to 7%.

C. Exclusion of adjacent-panel events

Certain correlations in the data, which will be discussed in the next section, lead us to also reject the area

TABLE II. Expected monopole signal size in pA based on model of Dewar most consistent with calibration data; table entries in bold type are for directly coupled signals.

Section No.	Panel No. 1	2	3	4	5	6	7	8
1	**174**	2	0	0	0	1	2	9
2	**134**	2	0	0	0	1	2	9
3	**130**	9	2	0	0	0	0	1
4	**161**	9	2	0	0	0	0	1
1	8	**182**	1	0	0	0	0	2
2	8	**147**	1	0	0	0	0	2
3	2	**152**	10	2	0	0	0	0
4	2	**197**	9	2	0	0	0	0
1	2	10	**183**	1	0	1	0	0
2	2	10	**141**	1	0	1	0	0
3	0	1	**137**	10	2	0	0	0
4	0	1	**169**	10	2	0	0	0
1	0	2	8	2	1	6	0	0
2	0	2	8	2	1	6	0	0
3	0	0	2	**162**	10	2	0	0
4	0	0	2	**216**	10	2	0	0
1	0	0	2	0	**189**	35	0	0
2	0	0	2	0	**149**	32	0	0
3	0	0	0	1	**143**	9	2	0
4	0	0	0	1	**177**	9	2	0
1	0	0	0	0	0	0	0	0
2	0	0	0	0	3	**246**	0	0
3	0	0	0	0	2	**142**	9	2
4	0	0	0	0	2	**189**	9	2
1	0	0	0	0	0	24	**178**	2
2	0	0	0	0	0	24	**136**	2
3	2	0	0	0	0	0	**133**	8
4	2	0	0	0	0	0	**164**	8
1	1	0	0	0	0	4	8	**157**
2	1	0	0	0	0	4	8	**127**
3	9	2	0	0	0	0	2	**131**
4	9	2	0	0	0	0	2	**170**

contributed by trajectories passing through inductors on adjacent panels. The calculation to exclude this area is only a simple approximation, since the full area will be used as the operation improves. We estimate the fractional reduction in area from a position perpendicular to the axis as the ratio of the cross section for trajectories excluding adjacent-panel events to that for trajectories including all events. This value is [21]

$$\frac{A'}{A}=(2+\sqrt{2})^{1/2}-1=0.848\ . \quad (1)$$

The ratio is, of course, different for trajectories which are not perpendicular to the detector axis. However, because the length of the detector is much greater than its radius, the ratio will be close to this value for most of the trajectories, and the area contributed by axial trajectories is small since the ends are not covered. This calculation includes no corrections for the unresponsive inductor segments.

We conservatively estimate the net active sensing area as the product of the active sensing area of 1.3 m^2 and the fraction of that area which does not include adjacent-panel events, 0.848. In this model our net active sensing area with the unresponsive inductor segments and corner events excluded is 1.10 m^2.

VI. DATA

Between 4 March 1987 and 1 September 1988, we obtained 7373.6 h of computer data files of which 6482.4 h were active sensing time. This active time corresponded to 88% of the computer data files, but to only 50% of the total elapsed time. The experiment was interrupted for a 5-month period by building remodeling and for intermittent periods because of problems with the liquid-helium refrigerator. During the active operation, we observed 43 single-channel offsets which did not correlate with disturbances in the anticoincidence data (Fig. 18). With this frequency of uncorrelated single-channel offsets (roughly one per 780 h of operation per channel), we expect an accidental coincidence to occur in a 10 sec window once every ~800 yr. The incidence of double-coincident offsets is much higher than this estimate. Four have already been observed (Table III); however, the magnitudes are inconsistent with a Dirac charge, and such offsets always occur in adjacent inductors. Since adjacent-panel events contribute only ~0.152 of the total sensing area, it is extremely unlikely that we would observe four such events without observing events of any other type. The probability is approximately $(0.152)^4$ or 0.0005. A more likely cause is mutual rf interference between SQUID's coupled through adjacent pickup coils. All four events were recorded in the first 221 days of operation, and none have occurred since the rf excitation frequency for each SQUID was adjusted to avoid mutual resonances. Nonetheless, we have discarded the area contributed by adjacent-panel events, reducing our quoted sensing area to 1.1 m^2.

TABLE III. List of double-coincident offsets observed to date. Three apparent double-coincident offsets could be explained by inductive coupling due to large signals in panel 2 and are treated as single offsets.

Time	date	Channel	Magnitude (pA)
5:50	24 July 1987	5	342
		6	58
4:47	27 July 1987	4	48
		5	139
18:11	18 August 1987	1	65
		8	149
21:26	1 October 1987	5	395
		6	73

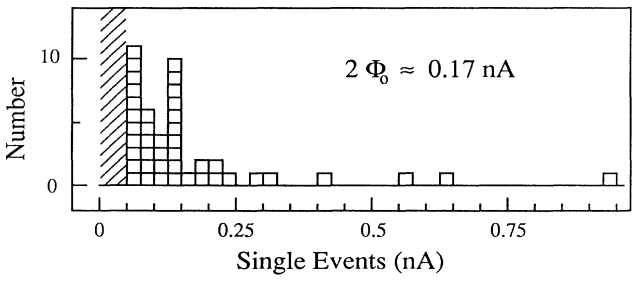

FIG. 18. Distribution of unexplained single-channel offset events above ~50 pA for all panels. The number of offsets from panels 1–8 is 7, 4, 5, 10, 9, 2, 3, and 3, respectively, for 43 total offsets.

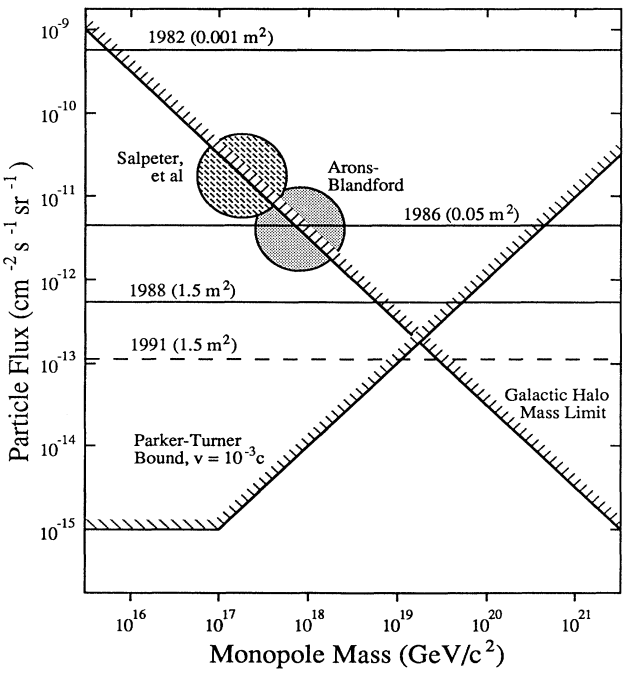

FIG. 19. Comparison of experimental and relevant theoretical limits on magnetic monopole flux in cosmic rays.

VII. CONCLUSIONS

With no candidate events observed, these data set an upper limit of 7.2×10^{-13} $cm^{-2}sec^{-1}sr^{-1}$ at 90% confidence level ($2.3/\int dA\, d\Omega\, dt$) on any uniform flux of magnetic monopoles passing through the Earth's surface at any velocity (Fig. 19). This limit is a factor of 2000 below the flux suggested by the single-candidate event seen with the prototype detector [2] in 1982. Based on this large factor and based on the noncoincident nature of the prototype detector, we conclude that the entire data set from the prototype detector which contains the single event should be discarded when quoting particle-flux limits for cosmic-ray magnetic monopoles. In addition, this new and lower flux limit is below the level suggested by the monopole plasma oscillation models, [22] largely ruling out these models. The new limit is also within a factor of ~5 above the peak created by the crossover in the mass-dependent Parker bound [23] and galactic dark-matter bound [24] at around the Planck mass.

ACKNOWLEDGMENTS

This research has been funded in part by Department of Energy Contract No. DE-AT03-82ER40-076.

APPENDIX A: DETECTOR RESPONSE MATRIX

1. Introduction

The calibration coils are configured to apply a known flux to two adjacent gradiometer halves simultaneously. If there were no coupling between adjacent gradiometers, the calibration coils would directly determine the detector response, since the flux applied to one gradiometer would not affect the signal observed in its neighbor. However, the inductive coupling between adjacent gradiometers is not negligible. As a result, we must develop a model which, given the response to flux applied to multiple gradiometers obtained from the calibration measurements, allows calculation of the response to flux applied to a single gradiometer half.

This appendix presents the model and notation used for these calculations. We then derive the equations governing the detector response and write them in matrix form. The appendix concludes with discussions of the modifications which model circuit defects resulting from open or shorted conductors and of the variational technique which determines some inductance parameters from the calibration data.

2. Model and notation

The model is a two-dimensional representation of the detector inductors, in which the detector has been unrolled to make all inductors coplanar (Fig. 20). Periodic boundary conditions are used. There are four interacting gradiometer halves ("sections") in each inductor, and we assume that the inductances between the gradiometer halves of each inductor and adjacent inductors are known and are the only coupling involved in the system. (Effects of shielding, the angle between inductors, and any other nonuniformities can be included in the model by modifying the appropriate inductances.)

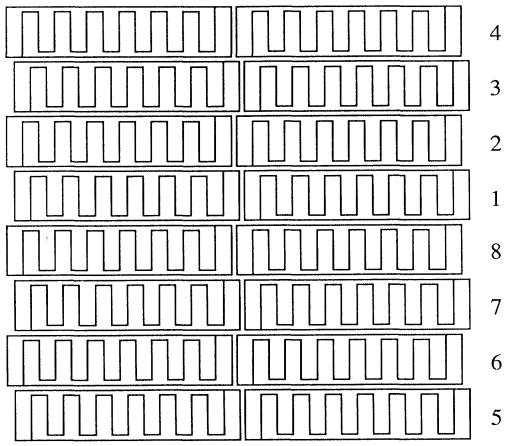

FIG. 20. Representation of detector coils in coplanar panel model with periodic boundary conditions. The SQUID's are located near right end of detector.

ϕ_{nj} is the flux in section j of inductor n, and i_{nj} is the current in section j of inductor n (Fig. 21). Here n ranges from 1 to 8 and j from 1 to 4. Hence the current through the SQUID connected to a given inductor is $I_{Sn}=\sum_{j=1}^{4} i_{nj}$. (Unfortunately, it is impossible to determine the individual currents i_{nj} with the present instrumentation.) S_{jk} is the mutual inductance between sections j and k of the same inductor, and M_{jk} is the mutual inductance between sections j and k of adjacent inductors. The first subscript refers to the inductor with lower index, and the second refers to the inductor with the greater index; for these purposes, 8 is less than 1. Here both j and k range from 1 to 4. Some of the symmetries for S_{jk} include $S_{jk}=S_{kj}$, $S_{jj}\equiv L$, $S_{12}=S_{34}\equiv M$, and $S_{13}=S_{24}$. Although M_{jk} is *not* transposable (M_{jk} is not equal to M_{kj} since the inductors are on different

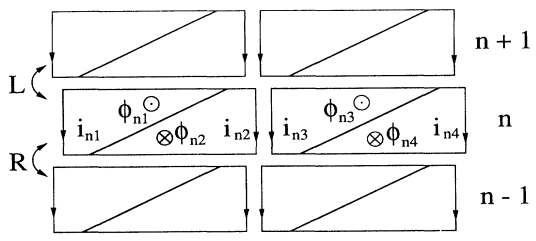

FIG. 21. Schematic of detector coils showing notation and conventions for positive fluxes and currents. The case shown is for odd n.

panels), it does have the following symmetries: $M_{11}=M_{22}=M_{33}=M_{44}$, $M_{12}=M_{34}$, $M_{13}=M_{24}$, $M_{21}=M_{43}$, and $M_{31}=M_{42}$. The asymmetry introduced by shifting the gradiometers along the axis of the detector results in two values for all M_{jk}, M^L_{jk} and M^R_{jk}, depending on whether the inductor with the greater index is shifted to the left or right, respectively. L_s is defined as the SQUID inductance and $L_{\rm tp}$ as the inductance of the twisted pair of leads which runs from each gradiometer to the SQUID.

3. Flux equations and inductance matrix

The equations describing the inductive coupling between a given section and all others to which it couples in this model are

$$\begin{aligned}\phi_{nj}=&i_{n1}(S_{j1}+L_s+L_{\rm tp})+i_{n2}(S_{j2}+L_s+L_{\rm tp})+i_{n3}(S_{j3}+L_s)+i_{n4}(S_{j4}+L_s)\\&+i_{n-1,1}M^R_{1j}+i_{n-1,2}M^R_{2j}+i_{n-1,3}M^R_{3j}+i_{n-1,4}M^R_{4j}\\&+i_{n+1,1}M^L_{j1}+i_{n+1,2}M^L_{j2}+i_{n+1,3}M^L_{j3}+i_{n+1,4}M^L_{j4}\quad (j=1,2)\end{aligned}\tag{A1a}$$

and

$$\begin{aligned}\phi_{nj}=&i_{n1}(S_{j1}+L_s)+i_{n2}(S_{j2}+L_s)+i_{n3}(S_{j3}+L_s+L_{\rm tp})+i_{n4}(S_{j4}+L_s+L_{\rm tp})\\&+i_{n-1,1}M^R_{1j}+i_{n-1,2}M^R_{2j}+i_{n-1,3}M^R_{3j}+i_{n-1,4}M^R_{4j}\\&+i_{n+1,1}M^L_{j1}+i_{n+1,2}M^L_{j2}+i_{n+1,3}M^L_{j3}+i_{n+1,4}M^L_{j4}\quad (j=3,4)\,,\end{aligned}\tag{A1b}$$

for odd n; for even n, the L and R values of M are interchanged. Defining the 4×4 matrices S and N,

$$S=\begin{bmatrix}L&M&S_{13}&S_{14}\\M&L&S_{23}&S_{13}\\S_{13}&S_{23}&L&M\\S_{14}&S_{13}&M&L\end{bmatrix}+\begin{bmatrix}L_s&L_s&L_s&L_s\\L_s&L_s&L_s&L_s\\L_s&L_s&L_s&L_s\\L_s&L_s&L_s&L_s\end{bmatrix}+\begin{bmatrix}L_{\rm tp}&L_{\rm tp}&0&0\\L_{\rm tp}&L_{\rm tp}&0&0\\0&0&L_{\rm tp}&L_{\rm tp}\\0&0&L_{\rm tp}&L_{\rm tp}\end{bmatrix},\tag{A2}$$

$$N=\begin{bmatrix}M_{11}&M_{12}&M_{13}&M_{14}\\M_{21}&M_{11}&M_{23}&M_{13}\\M_{31}&M_{32}&M_{11}&M_{12}\\M_{41}&M_{31}&M_{21}&M_{11}\end{bmatrix}.\tag{A3}$$

as well as the four-element flux and current vectors Φ_n and I_n,

$$\Phi_n=\begin{bmatrix}\phi_{n1}\\\phi_{n2}\\\phi_{n3}\\\phi_{n4}\end{bmatrix},\quad I_n=\begin{bmatrix}i_{n1}\\i_{n2}\\i_{n3}\\i_{n4}\end{bmatrix},\tag{A4}$$

the full system of equations is written compactly as $\Phi=M_D I$ or

$$\begin{bmatrix}\Phi_1\\\Phi_2\\\Phi_3\\\Phi_4\\\Phi_5\\\Phi_6\\\Phi_7\\\Phi_8\end{bmatrix}=\begin{bmatrix}S&N_L&0&0&0&0&0&N_R^T\\N_L^T&S&N_R&0&0&0&0&0\\0&N_R^T&S&N_L&0&0&0&0\\0&0&N_L^T&S&N_R&0&0&0\\0&0&0&N_R^T&S&N_L&0&0\\0&0&0&0&N_L^T&S&N_R&0\\0&0&0&0&0&N_R^T&S&N_L\\N_R&0&0&0&0&0&N_L^T&S\end{bmatrix}\begin{bmatrix}I_1\\I_2\\I_3\\I_4\\I_5\\I_6\\I_7\\I_8\end{bmatrix},\tag{A5}$$

where N^T is the transpose of the matrix N. The solution of this equation yields the output currents as a function of the input flux (whether from monopoles or calibration currents): $I=M_D^{-1}\Phi$.

In Appendix B we present calculations of the elements of the induction matrix. There is no significant difference between N_L and N_R, and most of the M_{jk} and a few of the S_{jk} are negligible.

4. Modifications for broken or shorted wires

The model can be modified to include the possibility of both short and open circuits in the detector gradiometers. In the run reported in this paper, we observed open circuits in two gradiometers.

Gradiometers which are shorted at the point where the leads join the gradiometers are modeled by removing the SQUID inductance from those terms of Eq. (A1) involving the current in the shorted sections. Also, the currents in the shorted gradiometers do not reach the SQUID, and so the current in a given SQUID is only the sum of the current in one gradiometer (i.e., $I_S=i_1+i_2$, not $I_S=i_1+i_2+i_3+i_4$, as is normally the case). If the short is not exactly at the point at which the leads are attached, the situation is more complicated. The gradiometer is now divided into two closed superconducting paths, one which includes the SQUID and one which does not. The signal which eventually reaches the SQUID will depend on the location of the short, through the relative sizes of the two loops created by the short. This case was not an-

alyzed in detail since it was not observed.

In the case of open circuits, the appropriate currents are set to zero. If an edge conductor is broken, the flux equation for that gradiometer half is replaced with the equation $i=0$, but the equation for the other half is unchanged. If both halves of a gradiometer do not respond to the calibration signals, there are two possible causes. Either the center conductor is broken, in which case $i_1+i_2=0$ replaces one flux equation and the difference of the original two flux equations ($\Phi_1-\Phi_2=\cdots$) replaces the other, or both edge conductors are broken, and both flux equations become $i_1=0$ and $i_2=0$. In the first case, a current can still flow in the perimeter wire and will couple to the adjacent gradiometers, but in the second case, it cannot. Data from calibration measurements can determine which fault condition occurred.

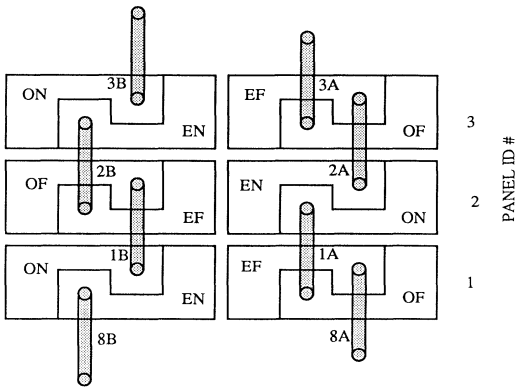

FIG. 22. Schematic diagram of calibration coil placement as it pertains to the coupling symmetries.

5. Variation of inductances

The above model does not predict all features of the observed calibration data. Since the interactions of the system can only be inductive, the actual inductances must be different from those calculated in Appendix B; we have discussed possible causes in the main body of this paper. This model of the system would also allow determination of the actual inductances, provided there were 32 linearly independent current/flux measurements (calibrations) *and* measurements of the 4 independent currents in each inductor. Each calibration would then be a column in the matrix I in the equation (all variables here are 32×32-element matrices) $M_D I=\Phi$. Then $M_D=\Phi I^{-1}$ and the calibration data determine M_D. Since this information does not exist, the discrepancy ($\sim10\%$) between the observed signals and those we would expect based on the inductance calculations of Appendix B must be resolved by other methods. We instead minimize the difference between the measured calibration data and the calculated calibration signals (in a least-squares value) by varying a few of the largest inductances (centered on the calculated inductances and chosen to match the observed coupling symmetries) and using the calculated values for the smaller couplings. Owing to the detector construction symmetries, certain inductances in our model are more likely to be in error than others and these are the values we vary.

The calibration data are a set of numbers which represent the response of the detector (i.e., eight SQUID currents) to currents applied to the 16 calibration coils. Although there are, in principle, a total of 128 values in each calibration run, most signals are below the noise level. Applying a flux equal to ten Dirac charges will produce signals above the noise level in four SQUID's: the two connected to the gradiometers to which the coil is directly coupled and the two connected to the adjacent gradiometers on either side.

The figure of merit is therefore the sum, over all *measurable* calibration signals, of the squares of the difference between the measured and calculated calibration signals. After adjusting the detector induction matrix for open-circuit sections, this figure of merit is calculated over a range of the selected inductances to find a minimum. Those inductances which yield the minimum deviation from the observed signals are used to calculate the response table for flux in the individual gradiometer half.

Based on trends observed in the data, along with consideration of the likely sources of perturbations to the inductances, the detector symmetry is broken by specifying separate values for the S_{ii}, S_{12}, and S_{34}, and varying these values. If the inductor index is odd, then $S_{11}\equiv L_{ON}$, $S_{22}\equiv L_{EN}$, $S_{33}\equiv L_{EF}$, and $S_{44}=L_{OF}$. (The subscripts N and F refer to whether the imbalanced gradiometer area is near to or far from the vertex between inductors crossed by the calibration coil in that gradiometer half, and the E and O refer to whether the identification number of the calibration coil itself is even or odd. (See Fig. 22.) Also, $S_{12}=M_N$ and $S_{34}=M_F$. For the inductors with an even index, the symmetry gives $S_{11}=L_{OF}$, $S_{22}=L_{EF}$, $S_{33}=L_{EN}$, $S_{44}=L_{ON}$, $S_{12}=M_F$, and $S_{34}=M_N$. The different definitions for odd and even inductors are required to accommodate the shifting of the gradiometers along the detector axis (See Fig. 20).

Even varying only these six parameters, the calculations are quite time consuming, as each point (that is, value of the figure of merit) in the six-dimensional space represents 16 solutions of a 32×32 matrix equation. As a result, the space is mapped first over a large area with a coarse grid, and followed by an increase in resolution over smaller areas near each successive minimum. The least-squares error varies slowly, and there is no risk of finding a local minimum rather than the global minimum. After reaching a certain resolution, the procedure ceases. The values of the inductances at the minimum determine the response of the detector to monopoles (see Table II).

APPENDIX B: CALCULATION OF GRADIOMETER INDUCTANCES

We first describe the general approach used to determine the gradiometer inductances. Some functions

necessary for efficiently describing the later calculations are defined next, followed by a derivation of the expressions for the self-inductance of a narrow ribbon and the self- and mutual inductances for two such ribbons whose spacing is the order of the width.

After these preliminary calculations, we characterize the inductance of the individual gradiometers. Calculations of the mutual inductances between gradiometers on adjacent panels conclude this appendix.

1. General

a. Basic theory and derivations

The self- and mutual inductances of the detector gradiometers are calculated using a method described by Grover [25] in which a complicated circuit is reduced to elements consisting only of straight filaments. The exact value of the mutual inductance of filamentary circuits is a double integral over the path of both circuits (A and B):

$$M_{AB}^{\text{fil}} = \oint\!\!\oint \frac{d\mathbf{l}_1 \cdot d\mathbf{l}_2}{|\mathbf{r}_1 - \mathbf{r}_2|} \ . \tag{B1}$$

The integral can be separated into contributions from the segments of each circuit. One such contribution could be written

$$M_{ij}^{\text{fil}} = \int_{\Gamma_1}^{r_f} \int_{\Gamma_2}^{s_f} \frac{d\mathbf{r} \cdot d\mathbf{s}}{|\mathbf{r} - \mathbf{s}|} \ , \tag{B2}$$

where Γ_1 and Γ_2 are the paths of segments Nos. i and j from each circuit and the integrals are along the current path. The total inductance of the circuit becomes

$$M_{AB}^{\text{fil}} = \sum_{i=1}^{N} \sum_{j=1}^{N'} M_{ij}^{\text{fil}} \ . \tag{B3}$$

This approach is particularly useful for circuits such as ours which consist entirely of segments whose inductances are easy to calculate (specifically, segments which are straight lines oriented at 0° or 90°).

For circuits of finite cross section, the filamentary inductances must be integrated over the cross section of each circuit, weighted by the normalized current densities $\mathbf{j}$:

$$M_{ij} = \int\int M_{ij}^{\text{fil}}(\mathbf{r}_1, \mathbf{r}_2)\mathbf{j}(\mathbf{r}_1) \cdot d\,\mathbf{A}_1 \mathbf{j}(\mathbf{r}_2) \cdot d\,\mathbf{A}_2 \ . \tag{B4}$$

Here r_1 and r_2 are the locations of the filaments in the plane of the cross sections [that is, M_{ji}^{fil} goes over to M^{fil} ($\mathbf{r}$ at i, $\mathbf{r}$ at j)].

Thus the equation for mutual inductance between two distinct circuits A and B is [26]

$$M_{AB} = \sum_{i=1}^{N} \sum_{j=1}^{N'} M_{ij} \ . \tag{B5}$$

In practice, the wires are *usually* much farther apart than their width and can be treated as filamentary ($M_{ij} \approx M_{ij}^{\text{fil}}$).

Note that perpendicular segments do not contribute since the scalar product vanishes [Eq. (B1)]. Also, for a given convention of positive current, the sign of M can be either positive or negative.

The self-inductance of the circuit is derived by setting $A = B$:

$$L = \sum_{i=1}^{N} \sum_{j=1}^{N} M_{ij} \ , \tag{B6}$$

where M_{ij} is the mutual inductance between the segments i and j, both on the same circuit. Of course, when $i = j$, the self-inductance of that element is used and is calculated from Eq. (B4) on identical cross sections. Divergences at zero filament separation are avoided in the integral form.

b. Useful equations

For each method it is useful to define a few basic functions to simplify the equations, programming, and understanding. They are derived by Grover [25], but listed here with names convenient for these calculations. For two parallel filaments of equal length s separated by a distance d and with both ends aligned [Fig. 23(a)]:

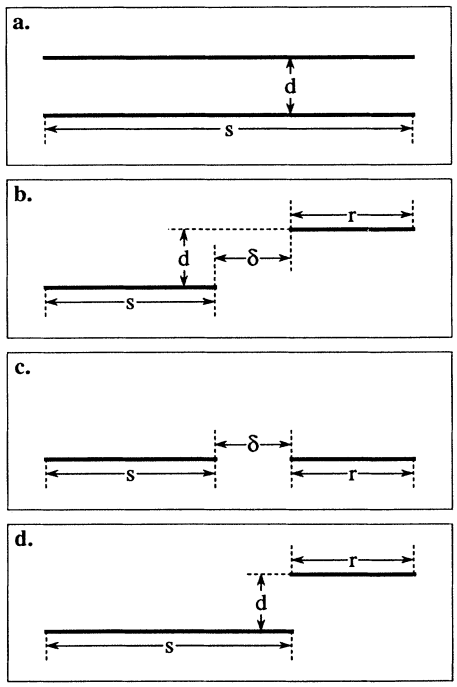

FIG. 23. Notation used in definitions of mutual inductances between parallel filaments. Currents are assumed to be parallel; if antiparallel, a negative sign is added to the function definitions. Functions are (a) $M_p(s,d)$, (b) $M_{\text{UP}}(s,r,\delta,d)$, (c) $M_{\text{SA}}(s,r,\delta)$, and (d) $M_{\text{UPT}}(s,r,d)$.

$$M_P(s,d)=k\left[s\,\text{arcsinh}\left[\frac{s}{d}\right]-(s^2+d^2)^{1/2}+d\right], \tag{B7}$$

where $k=0.002\ \mu$H/cm and all distances are in cm. The mutual inductance between two parallel filaments offset by δ and of unequal length [Fig. 23(b)] is $M_{\rm UP}$ (for unequal and parallel):

$$M_{\rm UP}(s,r,\delta,d)=\tfrac{1}{2}[M_P(s+r+\delta,d)+M_P(|\delta|,d)-M_P(|s+\delta|,d)-M_P(|r+\delta|,d)]\ . \tag{B8}$$

If the wires overlap, we write $\delta<0$, where $abs(\delta)$ is the distance of the overlap. The mutual inductance between two filaments on the same axis [Fig. 23(c)] is $M_{\rm SA}$ (for same axis):

$$M_{\rm SA}(s,r,\delta)=\frac{k}{2}[(s+r+\delta)\ln(s+r+\delta)-(s+\delta)\ln(s+\delta)-(r+\delta)\ln(r+\delta)+\delta\ln(\delta)]\ . \tag{B9}$$

Note that if the ends are touching, $\delta\ln(\delta)=0$, and this equation is still valid. The mutual inductance between unequal parallel filaments with the ends adjacent [Fig. 23(d)] is $M_{\rm UPT}$ (for unequal parallel tangent):

$$M_{\rm UPT}(s,r,d)=\tfrac{1}{2}[M_P(s+r,d)-M_P(s,d)-M_P(r,d)]\ . \tag{B10}$$

It is useful to define additional functions (in terms of the above functions) for the mutual inductances between rectangles in various orientations. The mutual inductance between filamentary boxes with the same height and in the same line [Fig. 24(a)] is $M_{\rm PB}$ (for parallel boxes):

$$\begin{aligned}M_{\rm PB}(a,b,c,x)=&M_{\rm SA}(a,c,x)-M_{\rm UP}(a,c,x,b)+M_{\rm SA}(a,c,x)-M_{\rm UP}(a,c,x,b)\\&+M_P(b,a+x)-M_P(b,a+c+x)+M_P(b,c+x)-M_P(b,x)\ .\end{aligned} \tag{B11}$$

The mutual inductance between boxes of nonsimilar dimensions which have the axis of opposite sides common [Fig. 24(b)] is $M_{\rm TB}$ (for tangent boxes):

$$\begin{aligned}M_{\rm TB}(a,b,c,d,x)=&M_{\rm UP}(a,c,x,d)-M_{\rm SA}(a,c,x)+M_{\rm UP}(a,c,x,b)-M_{\rm UP}(a,c,x,b+d)\\&+M_{\rm UPT}(b,d,a+x)-M_{\rm UPT}(b,d,a+c+x)+M_{\rm UPT}(b,d,c+x)-M_{\rm UPT}(b,d,x)\ .\end{aligned} \tag{B12}$$

The mutual inductance between nonsimilar rectangles with offsets from both axes [Fig. 24(c)] is $M_{\rm OB}$ (for offset boxes), which is the most general case:

$$\begin{aligned}M_{\rm OB}(a,b,c,d,x,y)=&M_{\rm UP}(a,c,x,d+y)-M_{\rm UP}(a,c,x,|y|)+M_{\rm UP}(a,c,x,b+y)-M_{\rm UP}(a,c,x,b+d+y)\\&+M_{\rm UP}(b,d,y,a+x)-M_{\rm UP}(b,d,y,a+c+x)+M_{\rm UP}(b,d,y,c+x)-M_{\rm UP}(b,d,y,|x|)\ .\end{aligned} \tag{B13}$$

This expression is also valid for boxes in which either x or y (but not both) is less than zero, but is not greater than either box dimension.

In applying any of these equations, the sign is reversed if one of the current is defined to flow in a direction opposite to those shown in the figures.

c. *Equations for thin strips of normal-metal conductors*

The cross section of particular interest in this experiment is that of a thin strip, similar to the ribbons used in the detector. We require both the self-inductance of a flat strip of superconducting wire and the mutual inductance between two such strips if their separation is similar to their width. Consider the general mutual inductance between two identical strips in the same plane separated by an arbitrary distance and with nonuniform current distributions. The mutual inductance for strips of length l is [Eq. (B4) and (B7)]

$$M=\int\int j(\mathbf{r}_1)j(\mathbf{r}_2)M_P(l,|\mathbf{r}_1-\mathbf{r}_2|)d^2r_1\,d^2r_2\ . \tag{B14}$$

The self-inductance is the above integral when both cross sections overlap fully; that is, they are the same conductor. In order to evaluate this equation, we form a series expansion for M_P in d/l to order $(d/l)^2$:

$$M_P(l,d)\cong kl\left[\ln\frac{2l}{d}-1+\frac{d}{l}-\frac{d^2}{4l^2}\right]\ . \tag{B15}$$

Substituting this approximation into the expression for M,

$$M=\int\int j(\mathbf{r}_1)j(\mathbf{r}_2)kl\left[\ln\frac{2l}{d}-1+\frac{d}{l}-\frac{d^2}{4l^2}\right]d^2r_1\,d^2r_2\ , \tag{B16}$$

where d is defined as the distance $|\mathbf{r}_1-\mathbf{r}_2|$. Three "mean distances" between the two wires (or between the wire and itself in the case of self-inductances) are the geometric mean R, the arithmetic mean δ, and the arithmetic mean square ϵ:

$$\ln R\equiv\int\int j(\mathbf{r}_1)j(\mathbf{r}_2)\ln d\,d^2r_1\,d^2r_2\ , \tag{B17a}$$

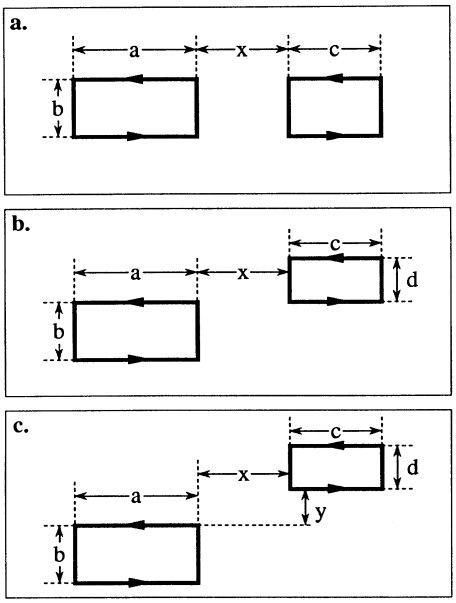

FIG. 24. Notation used in definitions of mutual inductances between coplanar boxes. Currents in both boxes are assumed to flow counterclockwise; if current in one box is reversed, a negative sign is added to the function definitions. Functions are (a) $M_{\mathrm{PB}}(a,b,c,x)$, (b) $M_{\mathrm{TB}}(a,b,c,d,x)$, and (c) $M_{\mathrm{OB}}(a,b,c,d,x,y)$.

$$\delta \equiv \int\int j(\mathbf{r}_1)j(\mathbf{r}_2)d\,d^2r_1\,d^2r_2\ , \tag{B17b}$$

and

$$\epsilon \equiv \int\int j(\mathbf{r}_1)j(\mathbf{r}_2)d^2\,d^2r_1\,d^2r_2\ . \tag{B17c}$$

In terms of these variables,

$$M \cong kl\left[\ln\frac{2l}{R}-1+\frac{\delta}{l}-\frac{\epsilon}{4l^2}\right]\ . \tag{B18}$$

If the current distribution is uniform, $j(r_1)=j(r_2)=1$ and the mean distances are (referring to Fig. 25 for the variable definitions) simply

$$\ln R=\frac{1}{a^2}\int_{(n-1)a/2}^{(n+1)a/2}\int_{-(n+1)a/2}^{-(n-1)a/2}\ln(x-y)dy\,dx \tag{B19a}$$
$$=\ln a-\tfrac{3}{2}+f(n)\ ,$$

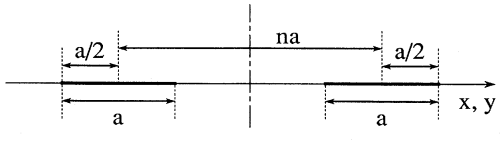

FIG. 25. Notation used in calculating the mean distances for thin strips. The value a is the strip width and n is the dimensionless separation normalized to a.

where

$$f(n)=\frac{(n+1)^2}{2}\ln(n+1)+\frac{(n-1)^2}{2}\ln|n-1|-n^2\ln n\ , \tag{B19b}$$

$$\delta=\frac{1}{a^2}\int_{(n-1)a/2}^{(n+1)a/2}\int_{-(n+1)a/2}^{-(n-1)a/2}|x-y|dy\,dx=na$$
$$(n\geq 1,\ \text{nonoverlapping strips})\ , \tag{B19c}$$

$$\delta=a(\tfrac{1}{3}+n^2-n^3/3)$$
$$(0<n\leq 1,\ \text{overlapping strips})\ , \tag{B19d}$$

$$\epsilon=\frac{1}{a^2}\int_{(n-1)a/2}^{(n+1)a/2}\int_{-(n+1)a/2}^{-(n-1)a/2}(x-y)^2dy\,dx$$
$$=a^2(n^2+\tfrac{1}{6})\ . \tag{B19e}$$

For self-inductances, $n=0$. Values for $n\neq 0$ are used for mutual inductances in a later section.

d. Self-inductance of isolated superconducting thin strips

The linear, normalized current density for an isolated superconducting strip is approximately [27]

$$j(x)=\frac{1}{\pi}\frac{1}{(w'^2-x^2)^{1/2}}\ , \tag{B20}$$

where w' is the width of half of the strip ($w'=w/2$) and x is the distance from the center. The values of R, δ, and ϵ are given by

$$\ln R=\frac{1}{\pi^2}\int_{-w'}^{w'}\int_{-w'}^{w'}\frac{\ln|x-y|}{(w'^2-x^2)^{1/2}(w'^2-y^2)^{1/2}}dx\,dy$$
$$=\ln\frac{w'}{2}=\ln\frac{w}{4}\ , \tag{B21a}$$

$$\delta=\frac{1}{\pi^2}\int_{-w'}^{w'}\int_{-w'}^{w'}\frac{|x-y|}{(w'^2-x^2)^{1/2}(w'^2-y^2)^{1/2}}dx\,dy$$
$$=\frac{8w'}{\pi^2}=\frac{4w}{\pi^2}\ , \tag{B21b}$$

and

$$\epsilon=\frac{1}{\pi^2}\int_{-w'}^{w'}\int_{-w'}^{w'}\frac{(x-y)^2}{(w'^2-x^2)^{1/2}(w'^2-y^2)^{1/2}}dx\,dy$$
$$=w^2=\frac{w^2}{4}\ . \tag{B21c}$$

Thus the self-inductance L_I of an isolated, flat superconducting wire of width w, negligible thickness, and length l is

$$L_I(l,w)=kl\left[\ln\frac{8l}{w}-1+\frac{4w}{\pi^2 l}-\frac{w^2}{16l^2}\right]\ . \tag{B22}$$

The mutual inductance between two flat superconducting wires which are sufficiently separated to be considered "isolated" strips will be taken as the mutual inductance between two filamentary wires, M_P in Eq. (B7).

e. Proximity effects

As a result of the perfect shielding which occurs in superconductors, the current distribution in superconduct-

ing wires in close proximity will not be represented by Eq. (B20). The redistribution of current will affect both the self- and mutual inductances of the wires, and unless the new current distribution is known, another method must be used to calculate the inductances.

The model for the system of two flat superconducting strips of width w in the same plane with a given separation is a system of two superconducting rings, both with the same diameter and axis and with the long dimension of the ring cross section parallel to the axis, as in a wedding band. The two major rings are each divided into $N/2$ minor rings [each of width $w/(N/2)$], which are assumed to have a uniform current density and the same quantum flux state as the original ring. The current in the major rings is distributed among the $N/2$ minor rings to maintain the constant flux, which models the superconducting state. The equations which govern the relations between the currents and fluxes in each minor ring include inductive coupling to all other minor rings in the system. The system is described by the equations

$$\Phi_k = \sum_{j=1}^{N} i_j M_{jk} \ . \tag{B23}$$

Φ_k and i_j are the flux and current in specified minor rings, and M_{jk} is the inductance between rings j and k. The sum is over both major rings, and so M_{jk} could be between minor rings on different major rings. If both indices are the same, the self-inductance for a normal ring replaces M_{kk}.

Since rings $k=1$ to $N/2$ and rings $k=N/2+1$ to N are part of the same superconductor, they will have the same flux in each; that is, $\Phi_k=\Phi_A$ for $k=1$ to $N/2$ and $\Phi_k=\Phi_B$ for $k=N/2+1$ to N. An additional constraint is that the net current in each ring is the sum of the current in all the minor rings:

$$I_A = \sum_{j=1}^{N/2} i_j \quad \text{and} \quad I_B = \sum_{j=N/2+1}^{N} i_j \ . \tag{B24}$$

The values for the individual currents are obtained by solving this matrix equation:

$$i_j = \sum_{k=1}^{N} M_{jk}^{-1} \Phi_k \ . \tag{B25}$$

Then the relation for I_A and I_B becomes

$$I_A = \sum_{j=1}^{N/2} \sum_{k=1}^{N} M_{jk}^{-1} \Phi_k \tag{B26a}$$

and

$$I_B = \sum_{j=N/2+1}^{N} \sum_{k=1}^{N} M_{jk}^{-1} \Phi_k \ . \tag{B26b}$$

Since the fluxes in the minor rings are equal to the flux in their respective major ring, this relation can be written

$$I_A = \sum_{j=1}^{N/2} \sum_{k=1}^{N/2} M_{jk}^{-1} \Phi_A + \sum_{j=1}^{N/2} \sum_{k=N/2+1}^{N} M_{jk}^{-1} \Phi_B \equiv R\Phi_A + S\Phi_B \ , \tag{B27a}$$

$$I_B = \sum_{j=N/2+1}^{N} \sum_{k=1}^{N/2} M_{jk}^{-1} \Phi_A + \sum_{j=N/2+1}^{N} \sum_{k=N/2+1}^{N} M_{jk}^{-1} \Phi_B \equiv T\Phi_A + U\Phi_B \ . \tag{B27b}$$

R, S, T, and U are constants, and Eqs. (B27a) and (B27b) form a 2×2 matrix equation. We invert this matrix and obtain the net flux in each ring in terms of the total current in each ring. However, this relation defines the self- and mutual inductances:

$$\Phi_A = L_A I_A + M_{AB} I_B \quad \text{and} \quad \Phi_B = M_{AB} I_A + L_B I_B \ . \tag{B28}$$

Since the major rings were identical, we will have $L_A=L_B\equiv L_N$ and $M_{AB}\equiv M_N$, where the subscript N refers to the near spacing.

In this manner we calculate the self- and mutual inductances for interacting superconducting rings for a fixed separation and fixed width. In practice, there were 30 minor rings in each major ring, resulting in a 60×60 matrix. This calculation need be performed only for the shortest segments of the gradiometers, since they are the only ones which approach closely enough for the shielding effects to become important (see Fig. 2).

Tests at zero separation with the formulas for mutual inductances between rings ($M=k2\pi r[\ln(8r/R)-2]$, valid for $w \ll r$ and with R defined as in Eq. (B21a)) confirm that the limiting case agrees with the formula for a single ring, $L=k2\pi r[\ln(32r/w)-2]$, where r is the radius and w is the width (again, for $w \ll r$) [28]. Since the conductors are not rings but flat strips, the strip inductances derived above are used in the initial inductance matrix rather than those of rings. Again, tests in the limit of zero separation confirm that this model produces reasonable results.

Calculations for the dimensions of interest in later calculations ($l=4.826$ cm, $a=0.2032$ cm, and edge-to-edge separation $=0.079$ cm) yield values of $L_N=0.0405$ μH and $M_N=0.0258$ μH.

Self- and mutual inductance of a single gradiometer

Each inductor contains two gradiometers wired in parallel, and each gradiometer in turn consists of two

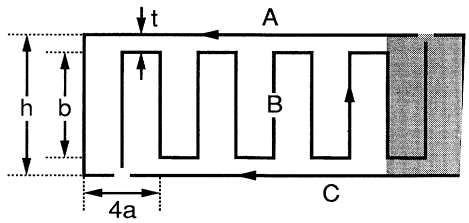

FIG. 26. Notation used in calculating the inductances of gradiometer sections. Upper case letters refer to wire segments; lower case letters are dimensions. The shaded area at right is one gradiometer "cell."

perimeter conductors and a meandering central conductor (Fig. 26). The region shaded in Fig. 26 is defined as one gradiometer cell, so that 27 cells comprise the full gradiometer. The self- and mutual inductances for a single gradiometer are the largest couplings in the system and are calculated here.

a. Notation

We calculate the inductances of the gradiometers using the method above, considering the self-inductance of each straight section of the gradiometer and mutual inductance between each pair of straight sections in the gradiometer. Identifying the three primary wires of the gradiometers as shown in Fig. 26.

$$L = L_A + L_B + 2M_{AB} \,, \tag{B29a}$$

$$M = M_{AB} + M_{AC} + L_B + M_{BC} = 2M_{AB} + M_{AC} + L_B \,, \tag{B29b}$$

where the subscripts now refer to the gradiometer wires. The values L and M are those defined in Appendix A for S_{jj} and S_{12}, respectively.

b. Calculations

The difference between h and b is small so the short segments of length t at the end of wire B are ignored when calculating the inductances:

$$L_A = L_C = L_I(2a(N-1),w) + L_I(h,w) + L_I(2a,w) - M_{\rm UP}(2a(N-1),2a,-2a,h) + (N/2-1)[L_N - L_I(2a,w)] \,, \tag{B30a}$$

$$L_B = (N-2)L_N + (N-1)L_I(b,w) + 2\sum_{i=1}^{N-2}(-1)^i(N-1-i)M_P(b,2ai) + 4\sum_{i=1}^{N/2-2}(N/2-1-i)M_{\rm SA}(2a,2a,2a(2i-1)) + 2\sum_{i=1}^{N/2-1}(N-1-2i)M_{\rm UP}(2a,2a,2a(2i-2),b) \,, \tag{B30b}$$

$$\begin{aligned} M_{AB} = M_{BC} = {} & \sum_{i=1}^{N/2-1}[M_{\rm UP}(2a,2a,4a(i-1),b+t) + M_{\rm UP}(2a,2a,4ai-2a,t)] \\ & - \sum_{i=1}^{N/2-1}[M_{\rm UP}(2a(N-1),2a,-4ai+2a,b+t) + M_{\rm UP}(2a(N-1),2a,-4ai,t)] \\ & - (N/2-1)[M_N - M_P(2a,t)] + \sum_{i=1}^{N-1}(-1)^i(M_{\rm UP}(h,b,-(b+t),2ai) \,, \end{aligned} \tag{B30c}$$

$$M_{AC} = M_P(h,2aN) - 2M_{\rm SA}(2a,2a(N-1),0) + M_{\rm UP}(2a(N-1),2a(N-1),-2a(N-2),h) + M_{\rm UP}(2a,2a,2a(N-2),h) \,. \tag{B30d}$$

The correction to the inductances for closely spaced wires of *unequal* length has been included as follows. Since the effect of shielding decreases rapidly with increasing separation, we assume the dominant contribution can be calculated as if the wires were isolated. We then subtract the unperturbed inductances (L_I or M_I) for the short sections and add the perturbed inductances (L_N or M_N) for the short sections in their place. The calculations yield values of $L = 10.01\ \mu$H and $M = 6.86\ \mu$H.

3. Mutual inductance between gradiometers on adjacent panels

In the design phase, we intended the adjacent gradiometers to be decoupled to the 1–5 % level. Offsetting adjacent gradiometers by one-quarter of a cell decreases the coupling, since flux from a single wire in one gradiometer couples antisymmetrically to the nearest cell in the adjacent gradiometer. There is another coupling introduced by the construction method, however. Ideally, the center wires would overlap the edge wires where they run parallel to the detector axis in order to minimize the area imbalance between gradiometer halves. To simplify construction there is a gap between conductors near the edge of the gradiometers. This gap significantly increases the coupling since it is an area attached to only one of the two gradiometer halves (it locally unbalances the gradiometer) and is the area nearest to the adjacent gradiometer. The models do not include the effects of the superconducting shield since the closest the shield comes to the wires is much farther away than the important distances between wires.

Restricting the coupling to that between adjacent gradiometers, there are 64 mutual inductances to calculate for each displacement symmetry (R,L). Luckily, many are identical from symmetry considerations, and changing the calculations for the R and L positions is trivial.

Three different methods are available to calculate the mutual inductance between various gradiometer sections. In some sense all are simpler than the previous calculations in that the distances are always large enough to ignore proximity effects (between wires) and there are no cases where self-inductances must be included. However, there are many more inductances to calculate, and so the

equations are lengthy. The first method is an approximation in which the gradiometers have infinite length. There are also two methods for calculating the inductances for the actual finite-length gradiometers in the planar approximation. One, for use with the larger inductances, is similar to the original sum-over-wires method, and the other, for use with the smaller inductances, approximates each gradiometer as a sum of rectangular loops for which the inductance is simple.

a. Infinite-length limits

These equations are useful in many respects. First, they are a limit against which to test the correctness of the numerical calculations. Second, they are quickly modified to test the effect of varying certain detector parameters. Finally, it is straightforward to estimate the effects of having the gradiometers meet at an angle instead of being coplanar. Unlike the calculations for finite-length gradiometers, in which including the angle between wires perpendicular to the detector axis can be complicated, these calculations are simplified since the interactions between these wires *exactly* cancel, and the inductances are still simple functions of the location of parallel wires.

The equations for the largest mutual inductances (M_{11}, M_{12}, and M_{21} in the notation of Appendix A, which are the only ones which can be calculated in the infinite limit) are [21]

$$M_{11}=\frac{kl}{4}\ln\left[\frac{(s+t)^2(s+t+b)^2(s+t+h)^2(s+t+b+h)^2}{(s+2h)^4(s+2t)(s+2t+2b)(s+2t+b)^2}\right], \tag{B31a}$$

$$M_{12}=\frac{kl}{4}\ln\left[\frac{(s+t)^4(s+t+b)^4}{s^4(s+2t)(s+2t+2b)(s+2t+b)^2}\right], \tag{B31b}$$

$$M_{21}=\frac{kl}{4}\ln\left[\frac{(s+t+h)^4(s+t+b+h)^4}{(s+2h)^4(s+2t)(s+2t+2b)(s+2t+b)^2}\right], \tag{B31c}$$

where l is the total length of the gradiometer.

The equations are written in terms of the parameters of Fig. 26, with the additional variable s representing the center-to-center separation between edge conductors of adjacent gradiometers. In the above equations, the gradiometers are assumed to be coplanar. Including the true geometry changes the values by less than 5%.

b. Mutual inductances under wire-segment method

Two methods were used for the numerical simulations. The one developed first sums the contributions of all possible pairs of individual filaments, just as in the original calculation of the self- and mutual inductances of an individual gradiometer. This method was sufficient for calculating M_{11}, M_{12}, and M_{21}, as verified by convergence tests against the limits in the previous section, but did not yield sufficient accuracy for the remaining, smaller inductances. The problem appeared to be round-off error in the cancellation of many nearly equal sized terms. As a result, we took a different approach for the smaller inductances, in which each complicated circuit is considered to be the combination of many simple rectangular loops. Currents in overlapping wires are in opposite directions and hence do not contribute to the inductance.

In the wire method, the total mutual inductance between the circuits shown in Fig. 26 is

$$M_{11}=M_{11}^{AA}+M_{11}^{AB}+M_{11}^{BA}+M_{11}^{BB}(\text{top horiz})+M_{11}^{BB}(\text{bottom horiz})+M_{11}^{BB}(\text{vert}), \tag{B32}$$

where M_{11}^{BB} has been written in three pieces owing to the complexity of this term.

The mutual inductance between the A wires in inductors $(n,1)$ and $(n+1,1)$ is the sum of the inductances between each pair of parallel wires:

$$\begin{aligned}M_{11}^{AA}=&M_{\rm UP}(2a,2a,-a,h+s)-M_{\rm UP}(2a,2a(N-1),-3a,2h+s)\\&-M_{\rm UP}(2a(N-1),2a,-a,s)+M_{\rm UP}(h,h,s,a)+M_{\rm UP}(2a(N-1),2a(N-1),-2aN+3a,h+s)\ .\end{aligned} \tag{B33}$$

The above was the simplest term, since the center wire did not contribute. The terms become progressively more complicated from this point since the central, winding wire (B) has many more elements than the outer conductors. Define $n\equiv N/2-1$. The mutual inductance between wires A in inductor $(n,1)$ and B in inductor $(n+1,1)$ is

$$\begin{aligned}M_{11}^{AB}=&\sum_{i=1}^{n}[M_{\rm UP}(2a,2a,4ai-5a,h+s+t+b)+M_{\rm UP}(2a,2a,4ai-3a,h+s+t)]\\&-\sum_{i=1}^{n}[M_{\rm UP}(2a(N-1),2a,-4ai+a,s+t+b)+M_{\rm UP}(2a(N-1),2a,-4ai-a,s+t)]\\&+\sum_{i=1}^{n}[M_{\rm UP}(h,b,s+t,4ai-a)-M_{\rm UP}(h,b,s+t,4ai+a)]-M_{\rm UP}(h,t+b,s,a).\end{aligned} \tag{B34}$$

The short segment of length t at the end of wire $1B$ is a small contribution to the sum and is ignored to simplify the sum. The contribution from wires B of inductor $(n,1)$ and A of inductor $(n+1,1)$ is

$$M_{11}^{BA}=\sum_{i=1}^{n}[M_{\rm UP}(2a,2a,4ai-3a,s+t)+M_{\rm UP}(2a,2a,4ai-a,s+t+b)]$$
$$-\sum_{i=1}^{n}[M_{\rm UP}(2a(N-1),2a,-4ai+3a,h+s+t+b)+M_{\rm UP}(2a(N-1),2a,-4ai+a,h+s+t)]$$
$$+\sum_{i=1}^{n}[M_{\rm UP}(h,b,s+t,4ai+a)-M_{\rm UP}(h,b,s+t,4ai+3a)]-M_{\rm UP}(h,b+t,s+t,3a)\ . \tag{B35}$$

Finally, the contribution from the two center conductors, wire B from inductor $(n,1)$ or $(n,2)$ and wire B from inductor $(n+1,1)$ or $(n+1,2)$ is quite complicated, since it involves many short elements in each wire. The contribution of the top row of horizontal wires on the lower segment $(1B)$ is

$$M_{11}^{BB}(\text{top horiz})=\sum_{j=1}^{n-1}\left\{\sum_{i=1}^{j}[M_{\rm UP}(2a,2a,4a(j-i)-a,s+2t+b)+M_{\rm UP}(2a,2a,4a(j-i)-a,s+2t)]\right.$$
$$\left.+\sum_{i=j+1}^{n}[M_{\rm UP}(2a,2a,4a(i-j)-3a,s+2t+b)+M_{\rm UP}(2a,2a,4a(i-j)-3a,s+2t)]\right\}$$
$$+\sum_{i=1}^{n}[M_{\rm UP}(2a,2a,4a(n-i)-a,s+2t+b)+M_{\rm UP}(2a,2a,4a(n-i)-a,s+2t)]\ . \tag{B36}$$

For the inductance between the top wire and the bottom row of wires of inductor $1B$,

$$M_{11}^{BB}(\text{bottom horiz})=\sum_{j=1}^{n-1}\left\{\sum_{i=1}^{j}[M_{\rm UP}(2a,2a,4a(j-i)+a,s+2t+2b)+M_{\rm UP}(2a,2a,4a(j-i)-a,s+2t+b)]\right.$$
$$\left.+\sum_{i=j+1}^{n}[M_{\rm UP}(2a,2a,4a(i-j)-5a,s+2t+2b)+M_{\rm UP}(2a,2a,4a(i-j)-3a,s+2t+b)]\right\}$$
$$+\sum_{i=1}^{n}[M_{\rm UP}(2a,2a,4a(n-i)+a,s+2t+2b)+M_{\rm UP}(2a,2a,4a(n-i)-a,s+2t+b)]\ . \tag{B37}$$

The wires perpendicular to those considered thus far may not be ignored this time, not because they interact with the above wires, but because their contribution does not drop out, since the length is finite. Their contributions are

$$M_{11}^{BB}(\text{vert})=\sum_{j=1}^{n-1}\sum_{i=1}^{n-1}(-1)^{i+j}M_{\rm UP}(b,b,s+2t,|2a(i-j)-a|)\ . \tag{B38}$$

The equations for the other inductor pairs include many of these same numbers owing to the symmetry. All terms must be calculated also for the opposite displacement symmetry, but this change is minor. We use the planar values for all distances except the separation between the gradiometers, which is corrected to the actual distance and is $s=0.41$ cm.

c. Mutual inductances with rectangular section method

When the above method was applied to some of the smaller inductances, there were convergence problems which were caused by the large number of small terms involved in the sum. To obtain numbers of a more consistent size, the gradiometer is divided into many rectangular loops, or boxes, of various sizes. There are places where the boxes overlap, but the currents are flowing in opposite directions, and so by superposition there must be no coupling from these segments. Hence it does not matter that they are in the model but not in the system. This method is simpler than using wires alone and might have been used for the above inductances too if they had been developed at the same time. As it happened, we only calculated smaller inductances when it became apparent the larger ones were not sufficient to ex-

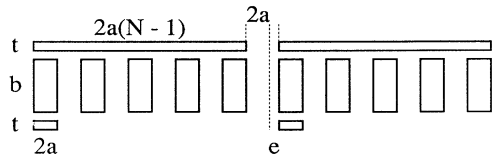

FIG. 27. Example of calculation of mutual inductances by the "box method." The boxes have been separated in the vertical direction for clarity.

TABLE IV. List of inductances in μH (high resolution).

Variable name	N_L value (μH)	N_R value (μH)
L	10.005	10.005
M	6.856	6.856
S_{23}	0.0686	0.0686
S_{13}	−0.0093	−0.0093
S_{14}	0.0044	0.0044
M_{12}	0.5338	0.5250
M_{11}	−0.3654	−0.3660
M_{21}	0.2758	0.2833
M_{23}	0.0140	0.0056
M_{13}	−0.0056	−0.0035
M_{14}	0.0035	0.0025
M_{32}	0.0057	0.0144
M_{31}	−0.0035	−0.0055
M_{41}	0.0024	0.0034

TABLE V. List of inductances in μH (values less than 0.02 μH are set to zero). Note that $N_L = N_R$ in this limit.

Variable name	N_L value (μH)	N_R value (μH)
L	10.01	10.01
M	6.86	6.86
S_{23}	0.07	0.07
S_{13}	0.00	0.00
S_{14}	0.00	0.00
M_{12}	0.53	0.53
M_{11}	−0.37	−0.37
M_{21}	0.28	0.28
M_{23}	0.00	0.00
M_{13}	0.00	0.00
M_{14}	0.00	0.00
M_{32}	0.00	0.00
M_{31}	0.00	0.00
M_{41}	0.00	0.00

plain the observations.

We demonstrate this method by calculating the value of M_{13}. Referring to Fig. 27, the mutual inductance between the long box on the left and all the boxes on the right is written as the sum of terms

$$\begin{aligned} M_\alpha = & M_{\rm PB}(2a(N-1),t,2a(N-1),2a+e) \\ & + M_{\rm OB}(2a(N-1),t,2a,t,2a+e,b) \\ & + \sum_{i=N/2}^{1} M_{\rm TB}(2a(N-1),t,2a,b,4ai-2a+e) . \end{aligned} \tag{39}$$

Note that the sum runs "backwards" from large i down to 1. The round-off error is minimized by adding the smallest terms first (at largest separation). The inductance between the smallest box on the left and all the boxes on the right is

$$\begin{aligned} M_\beta = & M_{\rm PB}(2a,t,2a,2a(N-1)+e) \\ & + M_{\rm OB}(2a,t,2a(N-1),t,2a(N-1)+e,b) \\ & + \sum_{i=N/2}^{1} M_{\rm TB}(2a,t,2a,b,2a(N-1)+4a(i-1)+e) . \end{aligned} \tag{B40}$$

The inductance between the row of boxes on the left with only the long and short boxes on the right is

$$\begin{aligned} M_\gamma = & \sum_{i=N/2}^{1} M_{\rm TB}(2a(N-1),t,2a,b,4ai-2a+e) \\ & + \sum_{i=N/2}^{1} M_{\rm TB}(2a,t,2a,b,4ai-2a+e) . \end{aligned} \tag{B41}$$

Finally, there is a term resulting from the interaction of one row of boxes with the other:

$$M_\delta = \sum_{i=N/2}^{1} \sum_{j=N/2}^{1} M_{\rm TB}(2a,b,2a,4a(i+j)-6a+e) . \tag{B42}$$

Thus the mutual inductance between the full gradiometer sections is the sum of these terms:

$$M_{13} = M_{24} = M_\alpha + M_\beta + M_\gamma + M_\delta . \tag{B43}$$

The calculation of other inductances between distant gradiometers follows this derivation closely.

4. Results of calculations

We now summarize the results of all inductance calculations. At first, we hoped that including the above couplings would be sufficient to explain the calibration results and thus calculated all terms S_{jk} and M_{jk} regardless of their size. These values are listed in Table IV, with the values for N_L in the left column and the values for N_R in the right column. Upon discovering that variations in the larger inductances of order 10% were needed to fit the calibration data, we used only the largest terms, those greater than 0.02 μH, in the variational calculations. These values are listed in Table V. Note that there is no longer any difference between N_L and N_R.

*Present address: Department of Physics, C. B. 172, University of Colorado at Denver, P.O. Box 173364, Denver, CO 80217-3364.

[1] For a recent review of theory, see J. Preskill, Annu. Rev. Nucl. Part. Sci. **34**, 461 (1984).

[2] B. Cabrera, Phys. Rev. Lett. **48**, 1378 (1982), and references therein.

[3] B. Cabrera, R. Gardner, and R. King, Phys. Rev. D **31**,

2199 (1985).
[4] B. Cabrera, M. A. Taber, R. D. Gardner, and J. Bourg, Phys. Rev. Lett. **51**, 1933 (1983); see also R. D. Gardner, B. Cabrera, M. E. Huber, and M. A. Taber, preceding paper, Phys. Rev. D **44**, 622 (1991).
[5] J. Incandela, M. Campbell, H. Frisch, S. Somalwar, M. Kuchnir, and H. R. Gustafson, Phys. Rev. Lett. **53**, 2067 (1984).
[6] S. Bermon, P. Chaudhari, C. C. Chi, C. D. Tesche, and C. C. Tsuei, Phys. Rev. Lett. **55**, 1850 (1985).
[7] M. W. Cromar, A. F. Clark, and F. R. Fickett, Phys. Rev. Lett. **56**, 2561 (1986).
[8] J. Incandela, H. Frisch, S. Somalwar, M. Kuchnir, and H. R. Gustafson, Phys. Rev. D **34**, 2637 (1986).
[9] S. Bermon, C. C. Chi, C. C. Tsuei, J. R. Rozen, P. Chaudhari, M. W. McElfresh, and A. Prodell, Phys. Rev. Lett. **64**, 839 (1990).
[10] M. E. Huber, B. Cabrera, M. A. Taber, and R. D. Gardner, Phys. Rev. Lett. **64**, 835 (1990).
[11] S. Somalwar, H. Frisch, J. Incandela, and M. Kuchnir, Nucl. Instrum. Methods **226**, 341 (1984).
[12] R. D. Gardner, Ph.D. thesis, Stanford University, 1988.
[13] Austenitic (300 series) stainless steel is weakly ferromagneic, however, and even the presence of a small amount of stainless-steel hardware may have been responsible for the discrepancy between the measured and calculated detector response which is discussed later.
[14] Teledyne Wah Chang, Albany, OR.
[15] R. P. Giffard, R. A. Webb, and J. C. Wheatley, J. Low Temp. Phys. **6**, 584 (1972).
[16] Sensors manufactured by Biomagnetic Technologies Inc. (formerly S.H.E.), San Diego, CA.
[17] Electronics manufactured by Quantum Design Inc., San Diego, CA.
[18] H. Frisch (personal communication).
[19] A. 0.05-Hz corner frequency was chosen since divergent low-frequency SQUID noise begins to dominate below this frequency. The signal-to-noise ratio is not increased by further reducing the bandwidth.
[20] The standard deviation for the difference between two random numbers is the standard deviation for a single distribution times $\sqrt{2}$, if they are independent. The size of a step offset is just such a difference.
[21] M. E. Huber, Ph.D. thesis, Stanford University, 1988.
[22] J. Arons and R. D. Blandford, Phys. Rev. Lett. **50**, 544 (1983).
[23] M. S. Turner, E. N. Parker, and T. J. Bogdan, Phys. Rev. D **26**, 1296 (1982).
[24] D. E. Groom, Phys. Rep. **140**, 325 (1986).
[25] F. W. Grover, *Inductance Calculations: Working Formulas and Tables* (Dover, New York, 1962).
[26] In sections of this appendix, intermediate results will sometimes use variables such as L, M, or M_{ij}, which are not the same as those in Appendix A. Final results are presented using the variables of Appendix A.
[27] V. L. Newhouse, *Applied Superconductivity* (Wiley, New York, 1964).
[28] S. B. Felch, Ph.D. thesis, Stanford University, 1984.

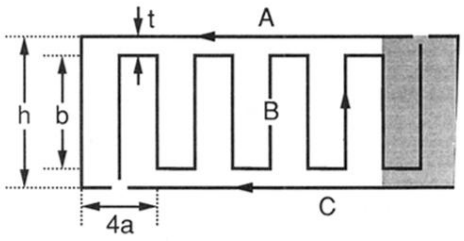

FIG. 26. Notation used in calculating the inductances of gradiometer sections. Upper case letters refer to wire segments; lower case letters are dimensions. The shaded area at right is one gradiometer "cell."

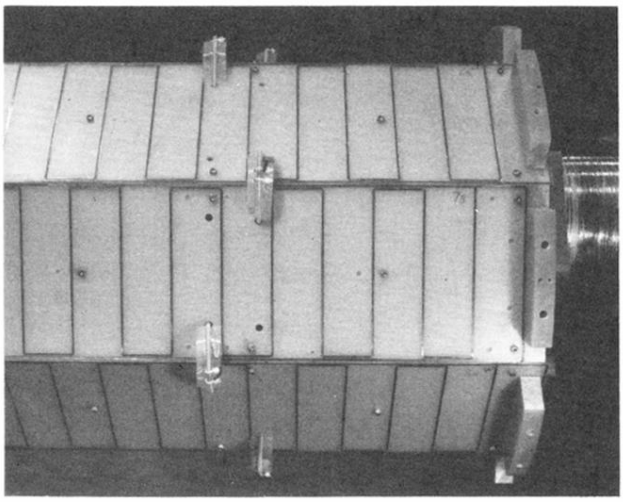

FIG. 3. Placement of calibration coils relative to the end of the detector.

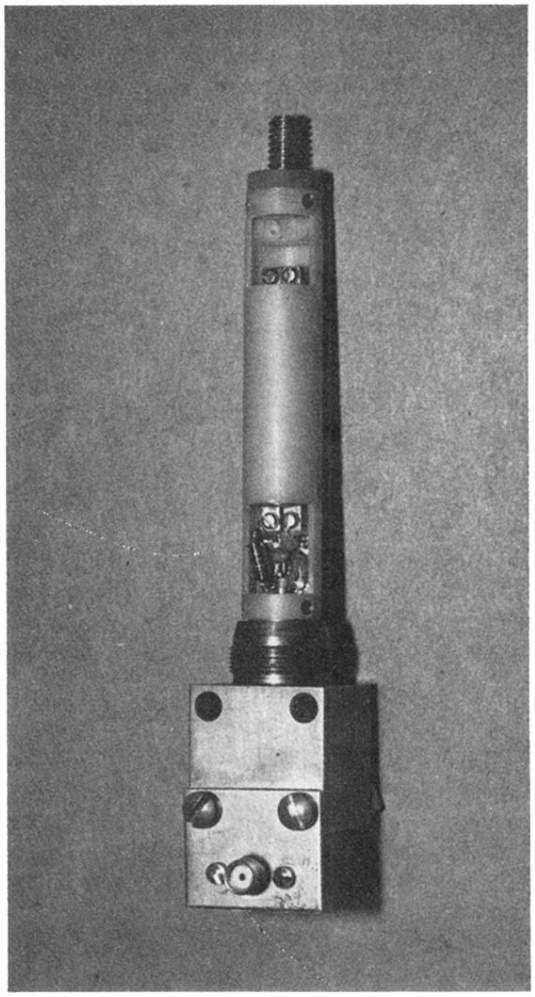

FIG. 5. SQUID housing and mounting assembly. Only the bias and input terminals of the SQUID are visible; the rest of the SQUID is hidden by the G-10 housing. The rf matching network is at the center of the photograph, and the brass cube at the bottom is used for mounting and heat sinking. The input leads enter the assembly through the hollow niobium screw at the top.

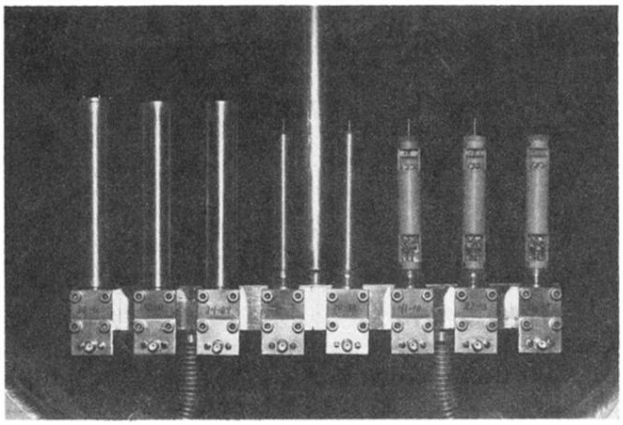

FIG. 6. SQUID's in various stages of assembly in position on the Dewar standpipe (used for cooling). SQUID's at right are in the same stage of assembly as shown in Fig. 5. At center, the niobium shield has been installed, and at left, the assembly is completed with a lead-plated brass cylinder.

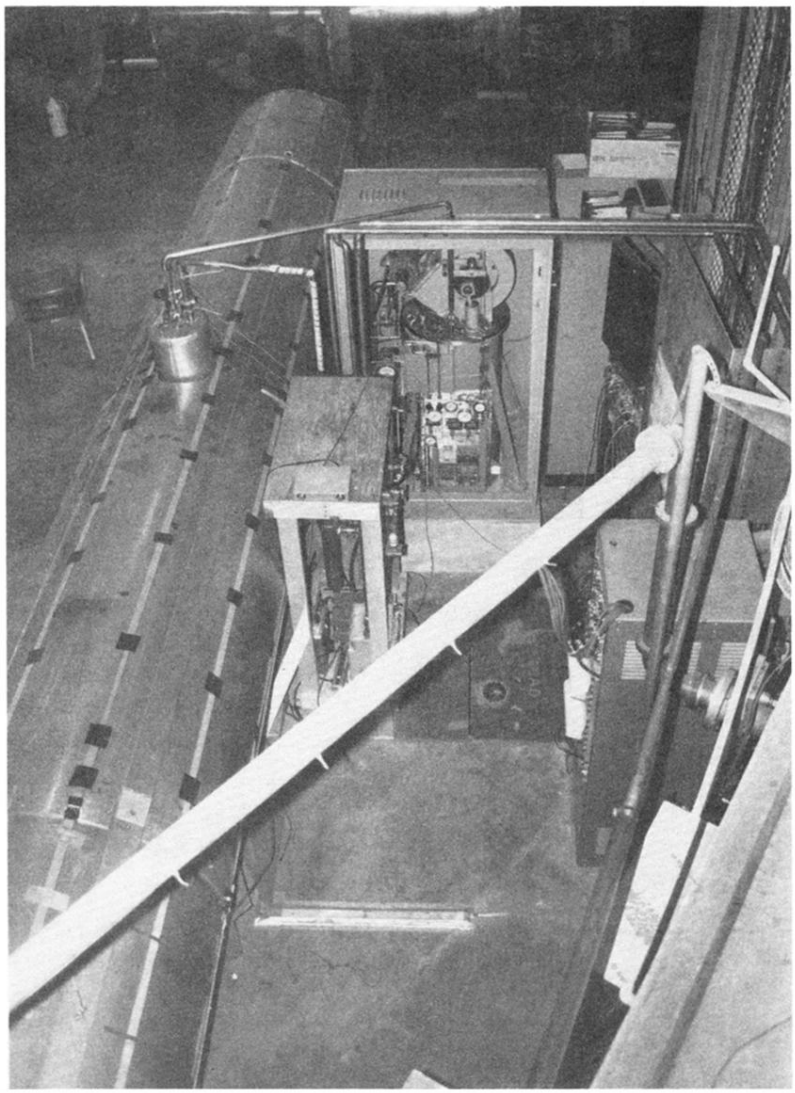

FIG. 7. Overview of detector laboratory. The helium liquefier is the large box at the center, and the shielded Dewar runs top to bottom along the left side of the picture. The ultrasonic motion detector is at the top of the wooden assembly in front of the liquefier and detects motion over an area from the front end of the Dewar to the electronics rack. The compressor for the liquefier is located behind the wall in the lower right corner.